Irregular Variability in Kepler Photometry

Master's Thesis
Submitted to Obtain the Degree of
Master of Science (M.Sc.) in
Physics (Nuclear, Particle and Astrophysics)

Martin Schlecker

December 16, 2016

Technical University of Munich
Physics Department

European
Southern Observatory

Max Planck Institute for
Extraterrestrial Physics

Assessors
Prof. Dr. Jochen Greiner (MPE)
Prof. Dr. Lothar Oberauer (TUM)

Supervisors
Prof. Dr. Jochen Greiner (MPE)
Dr. Valentin Ivanov (ESO)

In This Thesis:

The transit method is the most successful tool for exoplanet discovery to date. With more than half of all known exoplanets discovered by *Kepler* using this method, the mission also revealed a number of objects with dimming events that defy the common explanations, the most prominent being KIC 8462852 aka "Tabby's star". I embarked on a search for objects with such irregular transit signatures in the data of K2, the two-wheeled successor mission of *Kepler*.

My method is a combination of automated pre-selection of targets showing downward flux excursions and visual light curve inspection of the selected subset comprising about 1.5 % of the initial sample. In addition, I developed a tool to constrain the effective temperature of a planet-hosting star from photometry alone. This software finds broad application in any science case where a photometric spectral type estimate is necessary.

I used existing transit models and Bayesian inference to perform a Markov Chain Monte Carlo (MCMC) analysis of a planetary candidate I discovered. This putative gas giant is in a 1.32 d circular orbit with an exceptionally tight orbital radius of $a \approx 0.012$ AU. My analysis revealed a scaled planetary radius of $R_\mathrm{p}/R_\star = 0.0927 \pm 0.0026$ and an edge-on orientation with an inclination $i = 89.8^{+3.0}_{-3.4}$. EPIC 217393088.01 is one of the closest-orbiting exoplanets ever detected and the first giant planet with such a small orbital radius.

An additional major finding of my search is EPIC 220262993, which exhibits aperiodic, asymmetric dips in flux with rapid dimming rates and up to ~ 25 % depth, lasting for 2 d to 4 d. In previous works based on optical and mid-infrared photometry, this object was inconsistently classified as a possible quasar or a white dwarf. We conducted follow-up observations both photometrically with GROND on the MPI/ESO 2.2 m telescope in La Silla (Chile) and spectroscopically with FIRE on the Magellan/Baade 6.5 m telescope. With additional spectroscopy using ESI on the Keck II 10 m telescope we were able to distinguish between these cases: EPIC 220262993 is a quasar with redshift $z = 1.42$. This is the only known exemplar showing deep dips in flux on such a short time scale.

Contents

1. Introduction

Are we alone in the universe? This question is as old as mankind. Already our distant ancestors noticed a number of objects in the sky that behave differently than the rest. What drew their attention was the curious, irregular movement of these *asteres planetai*[1] across the canvas of fixed stars. For the Babylonians, they had to be gods. But soon the idea arose that the curious wanderers might be other worlds, similar to our own. Once we had the tools, we set out to study them and gradually assembled a picture of what lies beyond Mother Earth's surface. With the discovery of Pluto (Slipher 1930), then still considered a planet, the census of Solar System members was complete[2]. Today, we have established a clear distinction between distant stars and the nearby worlds that inhabit our home system.

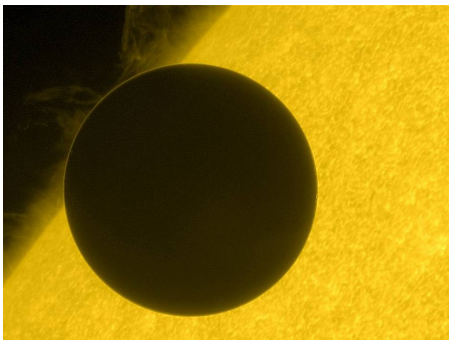

Venus transiting the Sun on June 5, 2012 as observed by Hinode's Solar Optical Telescope. On the upper left, a faint arc from refraction in Venus' atmosphere is visible. Credit: JAXA/NASA

However, as early as in the 16th century, Giordano Bruno formulated the idea that the fixed stars are similar to the Sun and likewise accompanied by planets (Bruno 1584). This possibility was passed on for centuries (e.g. Newton 1687), without a chance to obtain empirical evidence. It was clear that the detection of these worlds could not be achieved by conventional astronomical methods used for finding Solar System bodies, which were identified by detecting the sunlight reflected from their surfaces (Struve 1952). In today's exoplanetary science, we call this technique *direct imaging*.

The question of extrasolar systems remained, but it was not until 1995 that Bruno's suggestion became reality when Mayor & Queloz reported the discovery of 51 Pegasi b, the first known planet outside our home system orbiting a Sun-like star. It was found via the *Radial Velocity* (RV) method, where one measures the Doppler shift from small velocity changes of the host star that are caused by the gravitational pull of an orbiting secondary body. This discovery ignited one of the most substantial developments in astronomy in the last decades leading to the emergence of the fast-moving field of exoplanetary science. By the same technique, we learned only recently that the closest

[1] Greek: "wandering stars"
[2] However, see Batygin & Brown (2016) for evidence of the contrary

star to the Sun, Proxima Centauri, is orbited by a terrestrial planet (Anglada-Escudé et al. 2016).

While in the beginning RV was the predominant tool for finding new planets, it was soon joined by the *transit* method, which relies on precise measurements of the amount of light emitted by a star, and thus became only viable with a new generation of instruments with unprecedented precision (Sackett 1999). During a transit, a celestial body blocks part of the light emitted from a star when it passes in front of it. If such dips in brightness occur periodically, one can infer the presence of an opaque body orbiting this star. As the name suggests, an RV measurement only takes into account the radial component of the Doppler signal, i.e. an observer detects only the movement of the star along the line of sight (Struve 1952). Since there is no information about the relative inclination i of an unresolved system, such a measurement can only put an upper limit $M_\mathrm{p} \sin i$ on the planetary mass M_p. The only other knowledge about an RV planet are its orbital period P, its eccentricity e, and the argument of periastron ω (Kipping 2011).

In contrast, from transit photometry alone one can infer a number of additional properties. The shape of the transit signature contains information about the orbital period, radius, and inclination, the (scaled) planetary radius, and even about the brightness profile of the parent star due to stellar limb darkening (Sackett 1999, see Section 4.3.4). Transit light curve models can be used to characterize both a planet and its host star (Hubbard et al. 2001) and consequently yield constraints on planet formation (Cody & Sasselov 2002). If observed in more than one wavelength band, transit light curves can even reveal temperature profiles and atmospheric composition of planets (e.g. Seager & Sasselov 2000; Sing et al. 2011). With the harvest of thousands of new planets through the *Kepler* mission and its successor K2, the transit method has become the most successful tool planet hunters have at hand. For the first time, exoplanet scientists have a tool capable of detecting and characterizing Earth-sized planets around Sun-like stars (Koch et al. 2010). Designed specifically for this goal, the *Kepler* pipeline searches for transit signatures of planetary origin (Jenkins et al. 2010).

In addition to these "canonical" signatures, there have been discoveries of aperiodic dips in flux. A distinct class of objects with such features called "dippers" has been identified as being young low-mass stars with protoplanetary disks (e.g. Herbst & Shevchenko 1999). A similar behavior has recently been reported for the white dwarf WD 1145 + 017, which exhibits short, asymmetric dips of up to 40 % of the total flux that have been interpreted as transits of disintegrating planetesimals (Vanderburg et al. 2015a; Xu et al. 2016). One of the most confounding discoveries of *Kepler* is KIC 8462852, also known as Tabby's star, an apparently typical F3V star (Lisse et al. 2015) that shows completely unpredictable dimming events with a depth ranging from $\lesssim 1\,\%$ to more than 20 % (Boyajian et al. 2016). While dippers appear to be common (Ansdell et al. 2016), WD 1145 + 017 is the only observed object of its kind, and there is no analog for the anomalous dips of KIC 8462852 to date. The discovery of similar events would thus be a significant addition to the available sample. For this reason, I carried out a search for deep and aperiodic dimming events in the K2 long cadence database.

In this thesis, I report two discoveries and the methodology of their finding: First, a previously unknown short-period exoplanet candidate in the hot Jupiter regime. Second, a potentially extragalactic object that shows irregular dips in flux of up to $\sim 25\,\%$ on timescales of a few days. I give a brief overview with relevant background on transit photometry, the *Kepler* and K2 missions, and analysis techniques in Chapter 2. Chapter 3 deals with the software I developed for this project. Next, I describe the detection and investigation of the discovered transit events in Chapter 4. In Chapter 5, I discuss the implications of my findings and provide an outlook for possible follow-up actions.

2. Transit Photometry

Although extrasolar transits have only been detectable for a few decades, they already served as a tool in a variety of astrophysical subfields, ranging from exoplanet detection (e.g. Charbonneau et al. 2000) to stellar activity (e.g. Basri et al. 2011) to the search for time variations of the gravitational constant (Masuda & Suto 2016). This chapter is intended to provide background information to the main topic of my thesis project, which is the detection of transit events observed with the *Kepler* space telescope and their subsequent interpretation.

2.1. Transiting Exoplanets

Throughout this thesis, I make the reasonable assumption that the distance to an extrasolar system is much larger than the orbital radius of any bodies orbiting in this system. This entails an important implication: The light from a host star travels on parallel paths to us, and thus the missing flux δ due to the transit becomes independent of the orbital radius. Following Mandel & Agol (2002), I model transits of an opaque and dark sphere ("planet") that eclipses a spherical star. I will further assume a small planet-to-star ratio, $R_\mathrm{p}/R_\star < 1/2$, so that there is a finite time interval during which the planet's disk lies entirely inside the stellar disk if the transit impact parameter $b < 1/2\,R_\star$. Here, R_p and $R_\star$ are the planet and star radius, respectively. The overall shape of a transit event is then determined by four *contact points*, at which there is a discontinuity in the time derivative of the light curve (Kipping 2011, compare Figure 2.1). Points I and IV correspond to the times when the sky-projected distance d between host star and planet equals the sum of their radii, $d = R_\star + R_\mathrm{p}$. At the "inner" contact points II and III, we obtain $d = R_\star - R_\mathrm{p}$.

2.1.1. Observables and Science

If we are fortunate enough to observe the transit of an exoplanet, we obtain access to a wealth of information about the planet, its orbit around the host star, and the star itself. Transit photometry is also a very productive method to discover new planets (Winn 2010).

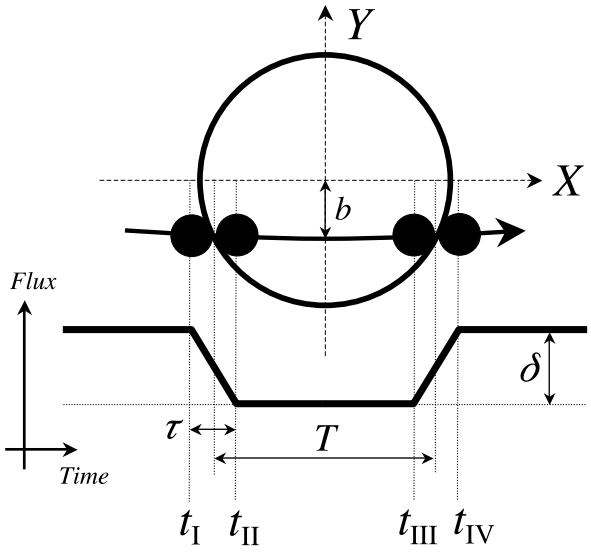

Figure 2.1.: Simplified transit geometry and light curve features. The schematic diagram illustrates the observation of a transit at the contact times t_{I} to t_{IV}. The transit duration T and the ingress and egress time τ of the corresponding light curve are largely determined by the impact parameter b. Credit: Winn (2010)

Orbit Orientation

The very fact that we observe a transit tells us that we look at the system nearly edge-on: Its inclination i must satisfy

$$r \cos i < R_\star + R_{\mathrm{p}}, \tag{2.1}$$

with the orbital radius r at the time of transit (adapted from Sackett 1999). With photometry sufficiently resolved in time and flux, we can infer additional information from the shape of the brightness dip; e.g. the shape of the ingress and egress phases further constrain i. For a planet with RV data, a measured inclination puts constraints on the planetary mass M_{p}, for which we get only a lower limit $M_{\mathrm{p}} \sin i$ from RV measurements alone (Boffin 2012).

Transit Depth

The incident flux F_0 from an isotropic, spherical radiation source is proportional to its projected circular area, $F_0 \sim R_\star^2 \pi$. Similarly, for a planet crossing the center of a stellar disk ($b = 0$) of uniform brightness, the missing flux during mid-transit obeys $\delta \sim R_{\mathrm{p}}^2 \pi$. For a Sun–Earth analog transit this amounts to 84 parts per million (ppm) (Koch et al. 2010). Hence, the transit depth is given by

$$\delta = 84\,\mathrm{ppm} \left(\frac{R_{\mathrm{p}}}{R_\oplus}\right)^2 \left(\frac{R_\star}{R_\odot}\right)^{-2}, \tag{2.2}$$

when expressed in terms of Earth radii $R_\oplus$ and Sun radii $R_\odot$, respectively. An absolute value for R_p can only be obtained if $R_\star$ is known, e.g. from stellar spectral typing or interferometric observations.

Transit Duration

The durations of planetary transits are usually of the order of a few hours, and they are separated by intervals lasting days to years. If the orbital period P of the planet is known, e.g. from observing multiple eclipses, the transit duration T can be calculated from the fraction of the orbital path for which the planet appears in front of the disk of its host star, which is the arc $\gamma_{I,II}$ between contact points t_I and t_IV. From geometric considerations (Sackett 1999), the transit duration for a circular orbit is

$$T = \frac{P\gamma_{I,II}}{2\pi a} = \frac{P}{\pi}\sin^{-1}\left(\frac{\sqrt{(R_\star + R_\mathrm{p})^2 - a^2\cos^2 i}}{a}\right). \tag{2.3}$$

If the semi-major axis a is much larger than the stellar radius $R_\star$, $\gamma_{I,II}$ can be approximated by a straight line of length $2R_\star$ (Haswell 2010). In this case, the transit duration approaches

$$T \overset{a\gg R_\star}{\approx} \frac{P}{\pi}\sqrt{\left(\frac{R_\star}{a}\right)^2 - \cos^2 i} \leq \frac{PR_\star}{\pi a}. \tag{2.4}$$

We can immediately see that the longest duration is reached at $b = a\cos i = 0$, i.e. with a perfect edge-on orientation of $i = 90°$. T also places a lower limit on the orbital period. From Kepler's third law,

$$P = \sqrt{4\pi^2 a^3/GM_\star}, \tag{2.5}$$

with the gravitational constant G and the stellar mass $M_\star$. This implies a lower limit on a as well.

Multiple Transits

If we observe more than one transit, we can directly infer the orbital period and use Equation 2.3 to determine i from the observed transit duration. Under the assumption that the geometry of the involved bodies and their orbits has not changed between two observations, we can improve the significance of the detection by folding the light curve about the period (compare Figure 4.3).

Wavelength-Dependent Signals

When observed in different wavelength bands, a transit signal can even reveal information about the temperature profile and atmospheric composition of a planet (Winn 2010). Researchers have just begun employing *Transmission Spectroscopy*, a technique that takes advantage of the wavelength-dependence of features in extrasolar atmospheres. The typical approach is to create wavelength-dependent light curves by using different

filters or a spectrograph, fit transit models to each of the light curves, and use the obtained wavelength-dependent transit depth $\delta(\lambda)$ to build a transmission spectrum (Winn 2010).

Using this young technique, researchers have been able to report temperature profiles (e.g. Sedaghati et al. 2016), to test the existence (e.g. Sing et al. 2011) or absence (e.g. Fischer et al. 2016) of atmospheric clouds and hazes, and to probe the chemical composition of exoplanet atmospheres (e.g. Evans et al. 2016). With the James Webb Space Telescope (JWST) operational within this decade, we can expect the detection of a large number of new molecular species and possibly even biosignatures (Seager et al. 2005).

Transit Timing and Duration

Another observable becomes available if more than two transit events can be detected. A variation of the times when the transits occur indicate gravitational perturbations from additional bodies in the system. These transit timing variations (TTVs) are generally of the order of a few seconds (Haswell 2010) and thus hard to detect. However, for planets in a mean motion resonance they can amount to several minutes. A number of planets have been found using this technique (e.g. Schmitt et al. 2014). TTVs, as well as variations of the transit duration (TDVs), are also discussed as a possible tool to detect extrasolar moons through their gravitational pull on the planet (Kipping 2011).

2.1.2. Characteristics of Host Stars

The information one yields from transit photometry in a single frequency band alone is limited. Absolute values for planetary parameters, and a complex understanding of an extrasolar system as a whole, can only be obtained with knowledge about the star within this system. Stellar properties depend mainly on the effective temperature $T_{\rm eff}$ and the surface gravity $\log g$, which enable us to estimate the stellar radius $R_\star$ and hence the size of an opaque transiting body. For the majority of K2's targets, and largely due to their faint apparent brightnesses, there are no spectra available that would enable a precise measurement of $T_{\rm eff}$. In Section 3.2, I introduce a tool that solves for the effective temperature using only photometric data in multiple bands, which are much easier to obtain than spectra. The program `TeffFit` fits photometry to template stars with known color-temperature relations.

2.1.3. Detectability of Transits

To evaluate the limits of photometric transit detection, we consider the case of a transiting exoplanet, which can be treated as the occultation of a circular disk by another much smaller one. The possibility of detecting an observed planetary transit depends on the photometric sensitivity of the instrument, on the properties of the transit event itself, and on the intrinsic stability of the host star. An instrument's sensitivity is largely limited by

the minimum difference in relative flux ΔF_{rel} that can be resolved. The most significant physical attributes of the transit are the apparent magnitude m and radius $R_\star$ of the host star, the radius of the planet R_{p}, the impact parameter b, and the transit duration T. I will ignore the third constraint for now; for the difficulties of detecting planets around active stars see Alonso et al. (2008).

Assuming that the cadence is high enough to detect even transits of short duration, i.e. the transit always consists of more than one data point, one can determine a lower detection limit for the planet-to-star ratio $R_{\mathrm{p}}/R_\star$. That means if we know the radius of a given host star, we can estimate how small a planet may be while still being detectable with K2 photometry. Comparing the right hand side of Equation 2.2 with the instrument's photometric sensitivity S, we find that the condition for detection is

$$S \overset{!}{\leq} \delta = \frac{R_{\mathrm{p}}^2}{R_\star^2}. \tag{2.6}$$

2.2. Analysis of Transit Events in a Bayesian Framework

In transit photometry, our data consists of a time series $\vec{y} = (y_1, \ldots, y_n)$ with measurements y_i at time t_i. We denote the predictions of a model by $\vec{f} = (f_1, \ldots, f_n)$, where $f_i = f(t_i, \theta)$ is the model function with a set of parameters θ. In practice, we have a fixed observed data vector $\vec{y}$ but unknown or insufficiently constrained model parameters θ. The probability density function (PDF) in this situation is called the likelihood function $\mathcal{L}(\theta)$ (Cubillos et al. 2016). This distribution function contains all of the evidence in a sample relevant to model parameters (G. A. Barnard 1962). In order to infer the best-fit parameters, we need to find the θ that maximizes the likelihood, i.e. $\hat{\theta} = \max_\theta \mathcal{L}(\theta)$. For the case of a Gaussian process with uncorrelated ("white") noise, the likelihood function becomes

$$\mathcal{L} = \prod_{i=1}^{n} \frac{1}{\sqrt{2\pi\sigma^2}} \exp\left(-\frac{(y_i - f_i)^2}{2\sigma^2}\right), \tag{2.7}$$

where the noise parameter σ specifies the width of the distribution. Maximizing this likelihood is equivalent to minimizing the chi-squared statistic

$$\chi^2 = \sum_{i=1}^{n} \left(\frac{y_i - f_i}{\sigma}\right)^2. \tag{2.8}$$

In transit photometry, σ is often estimated by measuring the standard deviation of the time series obtained when the transit not occurs. This approach describes the uncertainties of the data sufficiently only when the underlying noise process is Gaussian, stationary, and uncorrelated (Carter & Winn 2009).

2.2.1. Bayesian Inference

With the approach of Bayesian inference, new information updates the probability for a hypothesis. A prior distribution incorporates previous knowledge about the parameters of interest. We are interested in the posterior distribution, which is the conditional probability distribution on the parameter space given the observed data (Kipping & Sandford 2016). We obtain it by applying Bayes' theorem, where the posterior distribution is given by

$$P(\theta|\vec{y}) = \frac{P(\vec{y}|\theta)P(\theta)}{P(\vec{y})}. \tag{2.9}$$

Here, $P(\vec{y}|\theta)$ corresponds to the likelihood function $\mathcal{L}(\theta)$, and $P(\theta)$ is the prior probability distribution (hereinafter referred to as "prior"). The marginal likelihood or evidence $P(\vec{y})$ is often a complex integral. It is independent on θ and hence it is usually ignored for the task of parameter estimation. As a consequence, the posterior distribution is proportional to the product of likelihood and prior. The latter encodes the existing knowledge we have before the new data $\vec{y}$ is observed. By this dependence, Bayesian inference embodies Occam's razor by demanding extraordinary empirical evidence for extraordinary hypotheses (A. F. M. Smith 1980).

2.2.2. Prior Distributions

One can distinguish between informative and uninformative prior distributions. If the likelihood function is weakly informative compared to the prior, the posterior will have a high dependence on the prior. Such a likelihood is the case when considering low signal-to-noise ratio (SNR) data and motivates a careful choice of an informative prior. The contained prior knowledge can arise either from earlier studies or from theoretical predictions of observables (Feigelson & Babu 2012). If, on the other hand, the data has high SNR, it is justified to spend little effort on defining the prior and choose an uninformative distribution (Kipping & Sandford 2016). Uninformative priors assign equal probability to all possibilities, i.e. $P(\theta_i) = (b-a)^{-1}$ for a lower bound a and upper bound b of a single parameter θ_i. Often, a "flat" prior that assumes $a = -\infty$ and/or $b = +\infty$ is being used. This is technically an improper prior since $P(\theta_i)$, being a (normalized) probability distribution, equals to zero everywhere. However, when the posterior is obtained by a Monte Carlo sampling procedure, the acceptance probability is insensitive to a or b (compare Section 2.2.3). Thus, an improper prior can be a valid choice as long as the posterior remains proper (Kass & Wasserman 1996). Sometimes it is appropriate to deploy physical bounds for a and b, e.g. $0 < e < 1$ for the eccentricity of a closed orbit.

2.2.3. Monte Carlo Sampling

In a Bayesian framework, one can use repeated random sampling (referred to as Monte Carlo methods) to obtain credible regions for the parameters of a model. The goal

is typically to approximate the posterior distribution $P(\theta|\vec{y})$ of a set of parameters θ (compare Equation 2.9). Various strategies have been used to obtain a sample whose distribution is representative of this target distribution. A common approach is to sample from a proposal density $Q(\theta)$ that is similar to $P(\theta|\vec{y})$. This becomes difficult in cases where the shape of the posterior is complex or unknown. In this regard Markov chains, which represent a random walk with each state in $\{\theta^{(j)} \mid j \in 1, 2, ..., N\}$ only dependent on the previous step $\theta^{(j-1)}$ (Kroese 2011), have proved useful. A Markov chain is the core element of a Markov Chain Monte Carlo (MCMC) sampler, which generates a large number of random samples from the parameter space spanned by θ with a probability density that is proportional to the posterior (Cubillos et al. 2016). Thus, a histogram of the samples in the Markov chain approximates the posterior. In the limit $N \to \infty$, this histogram equals the target distribution (Kroese 2011). From Bayes' Theorem (Equation 2.9), we know that the evidence $P(\vec{y})$ is independent of the model parameters θ. Hence, there is no need to compute $P(\vec{y})$ unless one aims to compare the validity of different models (Kipping & Sandford 2016).

One of the most widespread MCMC techniques is the Metropolis-Hastings algorithm (Metropolis & Ulam 1949; Metropolis et al. 1953). In brief, it does the following:

1. Start at a position $\theta^{(j)}$ in parameter space where the posterior probability $P(\theta^{(j)}|\vec{y})$ can be computed
2. Draw a tentative next state $\theta^{(j+1)}$ from a proposal density $Q(\theta^{(j)})$ and compute $P(\theta^{(j+1)}|\vec{y})$
3. Compute the acceptance ratio $\alpha = \frac{P(\theta^{(j+1)}|\vec{y})}{P(\theta^{(j)}|\vec{y})}$.
   - If $\alpha > 1$, accept the new state and add the parameters $\theta^{(j+1)}$ to the Markov chain
   - If $\alpha < 1$, accept the new state with probability α
4. Repeat steps 2 to 4, until $j = N$

Note that $Q(\theta^{(j)})$ depends only on the current state. It can be any fixed probability density, it is not necessary that it is similar to the target density (MacKay 2005). The technique implies that successive samples are *not* independent from each other. To obtain a list of effectively independent samples from $P(\theta|\vec{y})$, the algorithm has to run for a large number of iterations. The convergence time especially suffers from parameters that are highly correlated among each other, which can lead to biased results (Maceachern & Berliner 1994). The autocorrelation of samples can be mitigated by *thinning* the Markov chain, i.e. keeping only every nth sample of the chain. We can measure the convergence of an algorithm, and thus estimate the required number of iterations, by determining the autocorrelation time (Foreman-Mackey et al. 2013).

Since a realistic MCMC procedure has a finite number of iterations, there is also a dependence of the approximated distribution on the starting point in parameter space.

To minimize the effect of initial parameters that were chosen far from the equilibrium distribution, one can discard an initial portion of the chain, the *burn-in phase*.

2.3. The *Kepler* Mission

The *Kepler* spacecraft was launched on March 6th, 2009 with the primary objective to search for Earth-like planets in the habitable zone of their host star by detecting transit signatures with high-precision time-series photometry (Borucki et al. 2005). This goal can be achieved by a parts-per-million photometric precision and a near-continuous cadence of $\sim 30\,\mathrm{min}$ (Koch et al. 2010). During its operational lifetime, *Kepler* observed a single 116 square degree field of view (FOV), which contains 223,000 stars with visual magnitudes $m_v < 14$ of all spectral types and luminosity classes. About 136,000 of them are estimated to be main-sequence stars (Monet 1996).

The *Kepler* mission yielded 4747 planetary candidates, of which 2331 have been confirmed as planets. 297 candidates and confirmed planets are in the habitable zone of their host star[1]. This makes *Kepler* the most successful planet finder mission to date.

In addition to exoplanet science, the data collected by *Kepler* bear scientific potential in other astrophysical fields such as asteroseismology (Bedding et al. 2011), stellar activity (Basri et al. 2011), binary stars (Thompson et al. 2012), and active galactic nuclei (Mushotzky et al. 2011).

2.3.1. Mission Architecture

Kepler's telescope has a 0.95 m aperture and a 1.4 m primary mirror. Its photometer consists of 21 modules, each with two 2200×1024 pixel CCD sensors with a full width at half maximum (FWHM) bandpass of 435 nm to 845 nm. The accessible dynamic range for the adopted integration time spans 9th to 16th magnitude stars. To reduce data traffic, exposures are combined into 29.424 min bins (long cadence) or 58.89 s bins (short cadence), and only "post stamp" images around objects on a predefined target list are downlinked. Their size and shape is chosen to maximize the SNR on typical exoplanet transit timescales of 3 h to 12 h (Thompson 2016, compare Figure B.2).

Kepler is in an Earth-trailing heliocentric orbit with a $\sim 372.5\,\mathrm{d}$ period. The observed star field is located near the galactic plane in the Cygnus region at RA = 19h 22m 40s, Dec = $+44°\,30'\,00''$ (see Figure 2.2). This pointing is 55° off the ecliptic plane, thus preventing the Sun from shining into the telescope at any time. In addition, the chosen target field inhibits occultations by Kuiper-belt objects and asteroids, which usually orbit in the ecliptic plane.

[1] as of November 17, 2016 (NASA Exoplanet Archive (Akeson et al. 2013), `http://exoplanetarchive.ipac.caltech.edu/`)

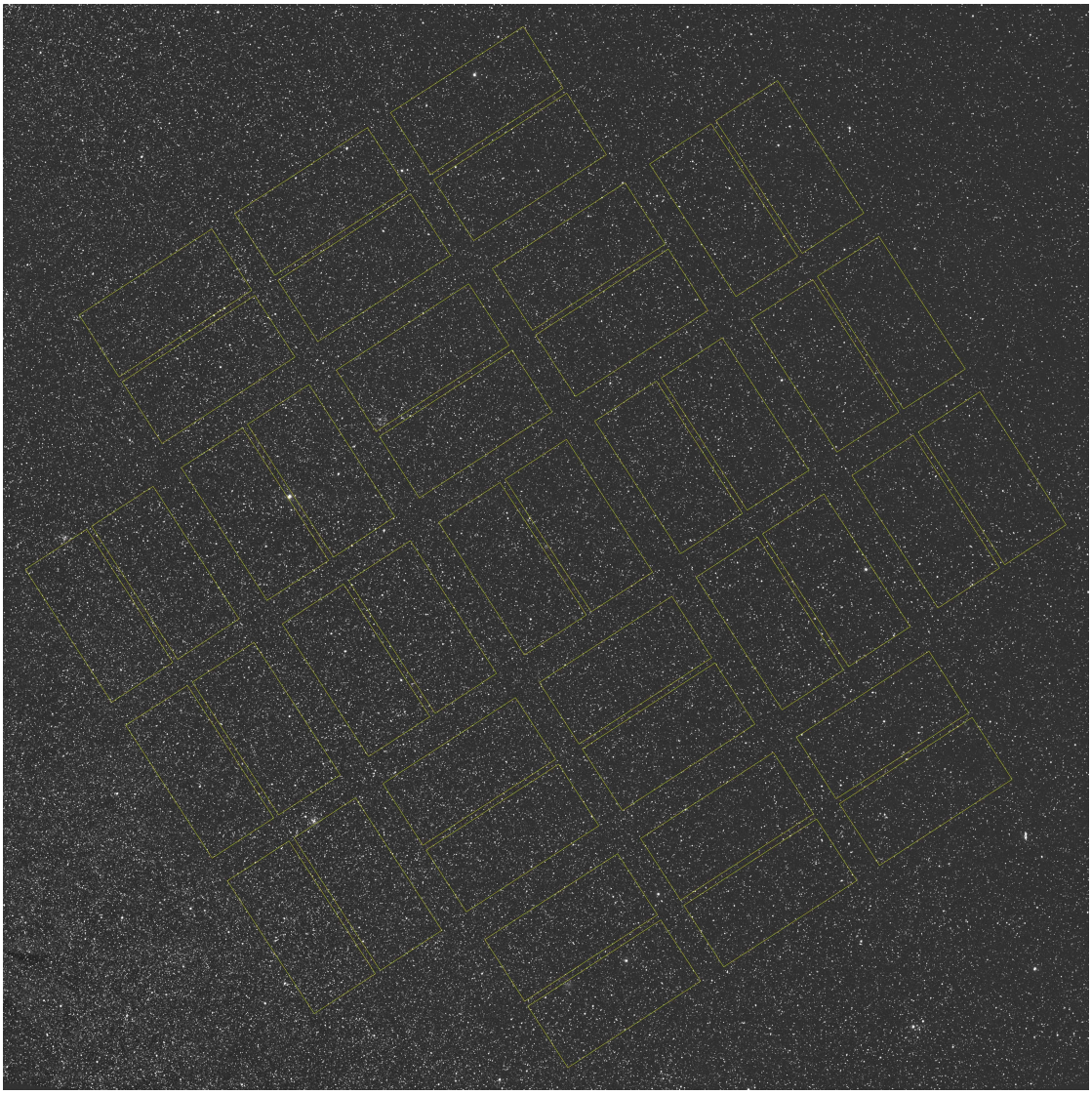

Figure 2.2.: *Kepler* field projected on the sky. The squares show the 21 detector modules, each consisting of two 2200 × 1024 pixel charge-coupled devices (CCD). The 106 square degree FOV contains 223,000 stars with $m_v < 14$ (Monet 1996). Image taken from ASAS survey, Pigulski et al. (2009).

2.4. *Kepler*'s Second Light: K2

A set of reaction wheels stabilized the accurate pointing of *Kepler* that was necessary to ensure its high photometric precision. The loss of a second reaction wheel in May 2013 lead to an early end of the original mission. Following this failure, a new operational concept was developed to enable the continuation of scientific observation. During the K2 mission, *Kepler*'s telescope observes sequential *Campaigns* of fields in the ecliptic plane (see Figure 2.3). With this pointing, the minimum allowed Sun angle limits the duration of each Campaign to approximately 80 d. Operating in the ecliptic plane minimizes the torque from solar wind pressure on the spacecraft. As a result, the pointing drift becomes small enough to be controlled by using the remaining two reaction wheels and performing regular thruster burns. For each Campaign, K2 targets are proposed by the scientific community in the Guest Observer program, in which questions from any area of astrophysics or planetary sciences can be addressed (Howell et al. 2014). All targets are listed in the Ecliptic Plane Input Catalog (EPIC, Huber et al. 2016). K2 is fully operational since June 2014.

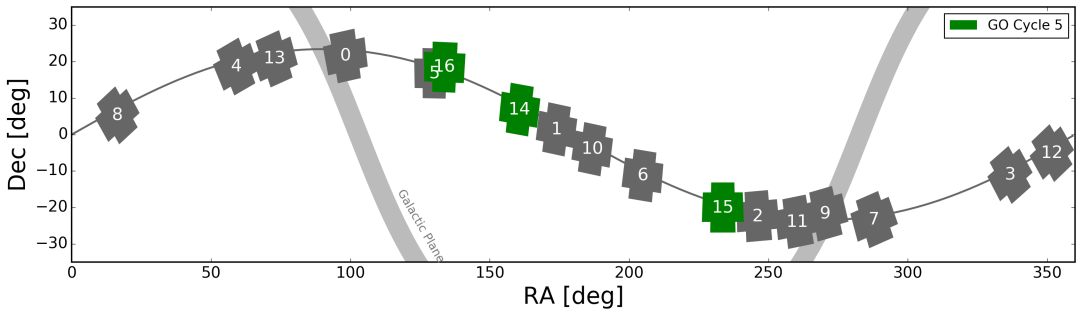

Figure 2.3.: Footprints of K2 Campaigns. The location and orientation of all conducted and planned Campaigns relative to the ecliptic (narrow line) are shown together with the Galactic plane (gray band). Credit: NASA Kepler & K2 Science Center

2.4.1. Photometric Performance

The precision of K2's photometry is not only restricted by the jitter of the spacecraft's boresight on timescales smaller than an exposure, but also by solar-induced motion and subsequent thruster firings on timescales longer than an exposure. These low-frequency disturbances cause targets to drift across detector pixels, resulting in a photometric precision of only 80 ppm for a 12th magnitude star on 6 h timescales (Howell et al. 2014, note that a smaller ppm value corresponds to higher precision). This means the performance for quiet G dwarfs is roughly a factor of four worse compared to the original *Kepler* mission. In order to mitigate these precision deficits, Vanderburg & Johnson (2014) make use of the predictability of the low-frequency pointing jitter and are able to correct

these systematics by applying a "Self-Flat-Fielding" (K2SFF) method. Subsequently, the photometric precision is improved by factors of two to five compared to raw K2 data (see Figure 2.4). Beginning with Campaign 3, an increase in pointing control bandwidth further improved precision to within a factor of two of *Kepler*'s.

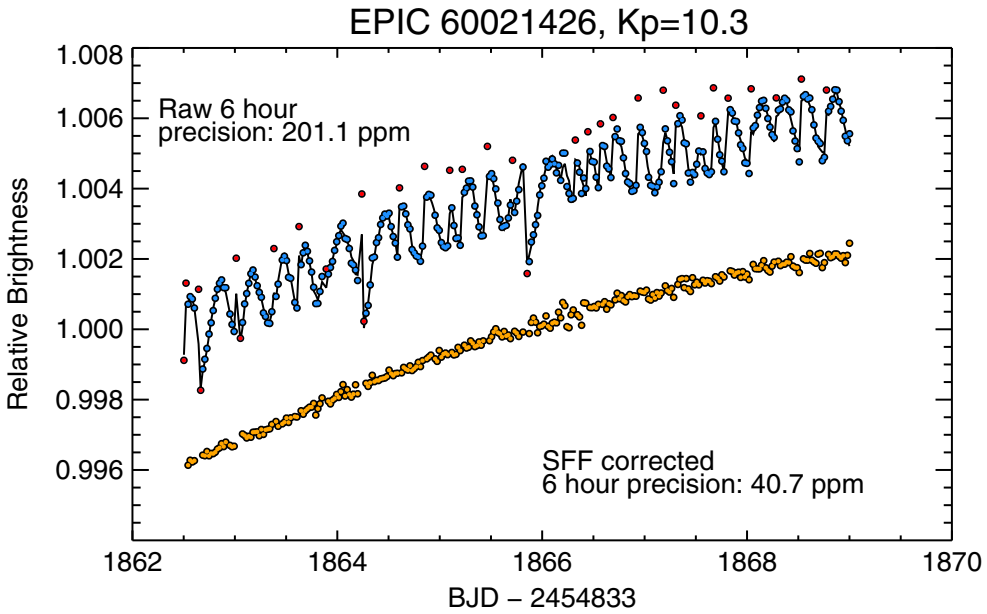

Figure 2.4.: Comparison between a raw K2 light curve and the corrected K2SFF photometry. Blue points indicate the light curve as obtained from the standard K2 pipeline. The black line underneath is the SFF model. Depicted in orange are the K2SFF corrected data resulting from the technique described in Vanderburg & Johnson (2014), vertically offset for clarity. Red points, which mark data taken during thruster firings, are excluded from the corrected light curve. The K2SFF corrected photometry shows substantial decrease in scatter compared to the raw data. Astrophysical features such as transits or starspot variations are preserved. Taken from Vanderburg & Johnson (2014).

Figure 2.5 provides a comparison between the computed photometric precision of K2 Campaign 3 (orange) and of *Kepler* quarter 10 (blue) with giant stars removed from the plot. It can be seen that K2's performance is generally lower than *Kepler*'s, but for stars of higher magnitude it approaches its precision.

2.4.2. Data Products

All K2 science data products in this overview can be accessed at the MAST[2]. Detailed information about the features of the K2 pipeline can be found in the *Kepler* Archive Manual (Thompson 2016). We can distinguish between pixel-level data, such as the

[2]Mikulski Archive for Space Telescopes, https://archive.stsci.edu

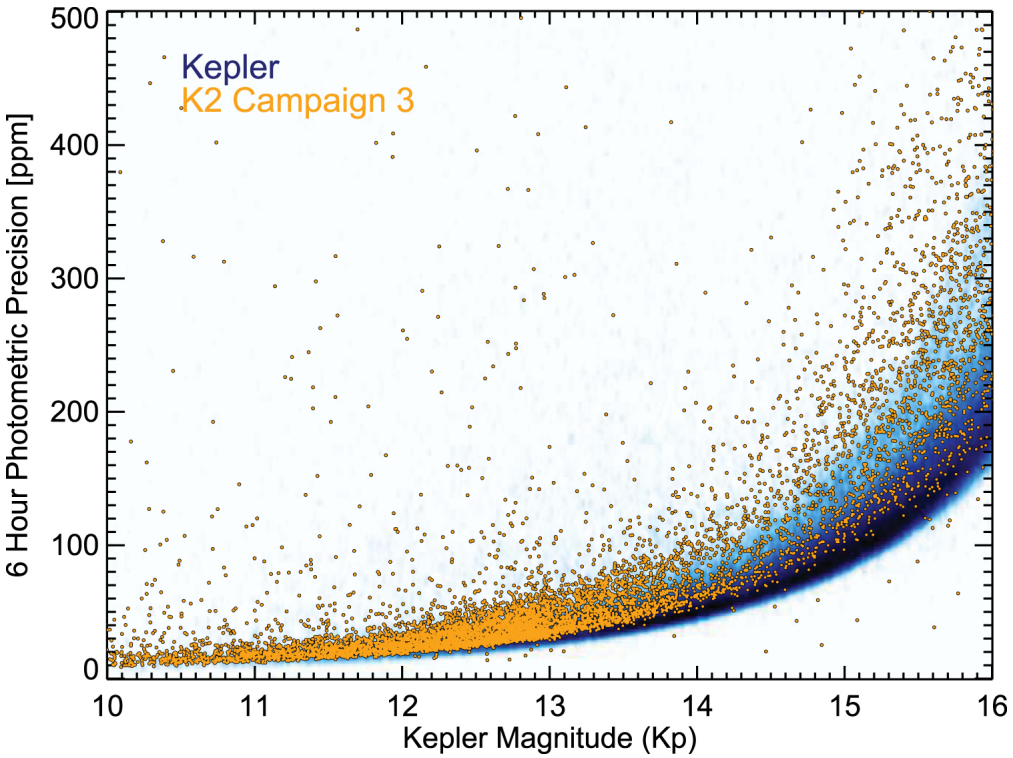

Figure 2.5.: Combined differential photometric precision of K2 and *Kepler*. Blue are stars observed during quarter 10 of the original *Kepler* mission. The fine-point precision from Campaign 3 is plotted in orange. Giant stars are excluded from the plot. For targets with $K_p \lesssim 13$, K2's precision approaches that of *Kepler*. Taken from Vanderburg et al. (2015b).

"raw" per-pixel time series, and High Level Science Products (HLSPs), e.g. processed light curves. As in the original *Kepler* mission, the majority of targets are observed in long cadence mode.

Target Pixel Files

Target pixel files contain time series of images, where each image is a single cadence. Hence, they provide individual photometric information for each pixel, which can be used to understand the results of the *Kepler* pipeline or to create custom light curves from the raw or calibrated data. The pipeline uses these data to create the HLSPs[3]. Target pixel files are available for short cadence and long cadence data.

PDC Time Series

Besides the inevitable statistical uncertainties, i.e. uncorrelated "white" noise, *Kepler*'s photometry is subject to systematic errors from the telescope and spacecraft, such as

[3]MAST Frequently Asked Questions, https://archive.stsci.edu/mast_faq.php?mission=K2, accessed 2016-10-23

thermal gradients or pointing drifts (Thompson 2016). The *Kepler* pipeline provides a HLSP with "detrended" photometry corrected for these trends. These Pre-Search Data Conditioning (PDC) light curves represent the flux contained in the optimal aperture given in electrons per second, after the pipeline applied its cotrending algorithm to correct for systematic spacecraft-related errors (Quintana et al. 2010). The time values correspond to the mid-point of a cadence in *Kepler* Barycentric Julian Day (BKJD, see Thompson 2016). Besides the flux time series, this product provides additional information about the target, the used CCD, and quality information for every data point.

K2SFF light curves

The user-provided K2SFF photometry is the result of a detrending approach described in Vanderburg & Johnson (2014). Light curves were extracted using a variety of photometric apertures, including a "best" aperture that results in the lowest root mean square (RMS). Usually, the photometry shows less systematics than PDC time series and it has substantially higher precision than the raw data (compare Figure 2.4). The K2SFF product does not contain uncertainty information and is released later than the pipeline products for a given Campaign.

EVEREST

EPIC Variability Extraction and Removal for Exoplanet Science Targets (EVEREST) is a user-contributed pipeline that uses pixel level decorrelation and a Gaussian process to remove spacecraft-induced systematics. It provides detrended light curves and additional photometric diagnostics (Luger et al. 2016).

Other Data Products

The MAST hosts additional science products such as full frame images, background pixel files, cotrending basis vectors, and collateral files for long and short cadence photometry. Software tools for data reduction and analysis, including my dip detection package `lcps` (see Section 3.1), can be obtained from the Kepler & K2 science center[4].

2.5. Irregular Transits in K2 Photometry

Transiting planets are usually found by planet-search algorithms tailored to search for characteristic signatures in a set of light curves. Several search methods have been successfully applied, most of them involve a search in the frequency domain (e.g. Fourier or Wavelet transforms, Hartman & Bakos 2016; Lomb-Scargle periodograms, Lomb 1976), often combined with fitting simplified (Box-Least-Squares, Kovács et al. (2002)) or realistic (Mandel & Agol 2002) transit models to the photometry. These algorithms are specifically tuned to find the periodic features of planetary transits. They are often not

[4] https://keplerscience.arc.nasa.gov/software.html

sensitive to asymmetric, distorted, or non-periodic dips. Such signals, however, have been found in *Kepler* and K2 data. Ansdell et al. (2016) report aperiodic dimming of young stellar objects (YSOs) observed in K2 Campaign 2 and relate it to the presence of protoplanetary disks. Another exotic example is the white dwarf WD 1145+017, which is being transited by one or several disintegrating planetesimals (Vanderburg et al. 2015a). More recently, there have been discoveries of deep dips in light curves of YSOs and young main-sequence stars that were explained by occultations from a circumstellar disk (e.g. McGinnis et al. 2015; Scaringi et al. 2016), transiting clumps of circumstellar material (Ansdell et al. 2016), or the transit of a large comet family (Bodman & Quillen 2016). The latter is also one of many discussed explanations for a most confounding *Kepler* discovery: the unaccountable flux variabilities of KIC 8462852 (Boyajian et al. 2016). While this object appears to be a common F3V star (Lisse et al. 2015), its light curve shows a number of significant dips. These dips occur in several periods of the four-year *Kepler* mission and are aperiodic, irregular in shape, and their depth varies from fractions of a percent up to $\sim 20\,\%$. Boyajian et al. present different models to explain the data, the most preferred being a transiting family of comets or planetesimal fragments. This explanation of KIC 8462852's light curve is challenged after Schaefer (2016) recently found a long-term dimming of $0.341\,\%\,\mathrm{yr}^{-1}$. The trend was confirmed for the duration of the *Kepler* mission by Montet & Simon (2016) and is followed by a rapid decline in flux of $> 2\,\%$ within 200 days.

2.5.1. Detection of Aperiodic Dimming Events

Such irregular dimming events are not readily found by planet-search algorithms. A different approach is to visually inspect light curves and spot suspicious dips after performing only minor corrections to the raw photometry. This technique takes advantage of the exceptional pattern-recognition ability of the human brain. Its value was for example proven in the citizen science project "Planet Hunters", which engages the public in a search for exoplanets in *Kepler* and K2 data. This project has been successful in finding planets (Fischer et al. 2012; Lintott et al. 2013; Schmitt et al. 2014), eclipsing binaries (EBs) (LaCourse et al. 2015), and as of yet unclassified signatures such as KIC 8462852 (Boyajian et al. 2016).

Because of the large number of long cadence targets observed during a K2 Campaign, I decided to follow a two-stage approach: First, I designed an algorithm which scanned through the complete sample of a Campaign and flagged prolonged downward excursions in the light curves (see Section 3.1). In a second step, I visually inspected the light curves that include detected dimming events and decided if they are candidates for further investigation (see Section 4.2).

3. Software Development

I developed my own software for the data analysis tasks related with the goal of my project. This chapter describes `lcps`, a package to search for transit-like features in light curves (Section 3.1) and the `TeffFit` tool, a Monte Carlo algorithm to fit photometry to template stars (Section 3.2). Both pieces of software are written in Python and follow an open source model. While `TeffFit` is work in progress and may be tested on request, `lcps` is already publicly available on the Python Package Index (PyPI) and at the Kepler & K2 Science Center[1].

3.1. Light Curve Pre-Selection

In the search for irregular transit signals, I wanted to reduce the target list to a number that makes visual investigation realistic. The idea was to sort out light curves that do not show any potentially interesting features. I created a Python-based tool `lcps` for this light curve pre-selection. The publicly available package searches for transit-like signatures (i.e. dips) in photometric time series. It uses the *Sliding Window* technique described below to compare a section of a light curve with its surroundings. A dip is detected if fluxes within this window are lower than a threshold fraction of the surrounding fluxes. Pre-selection algorithms like `lcps` will become increasingly important, given the data volumes expected from future exoplanet surveys such as TESS (Ricker et al. 2014) or PLATO (Rauer et al. 2016).

3.1.1. Extraction of Light Curves

Flux time series are either extracted from the PDC data product or from K2SFF files (compare section 2.4.2). From the FITS[2] files of PDC photometry, I extract the EPIC ID, the time data in BKJD, the PDC fluxes, and the flux uncertainties.

When working with the K2SFF product, I download the "best aperture" photometry of complete Campaigns in ASCII[3] format. From these files, `lcps` extracts the EPIC ID, the

[1] `https://keplerscience.arc.nasa.gov/software.html`
[2] Flexible Image Transport System
[3] American Standard Code for Information Interchange

time data in BJD[4]−2454833, and the relative flux. There is no uncertainty information in the K2SFF product.

3.1.2. Sliding Window Technique

`lcps` searches for dips of unknown depth and length. In order to detect as many ambiguous events as possible, I demand only few requirements on their shape. A dip event

- is a downward excursion from the surrounding fluxes.
- exceeds a defined amplitude.
- has a specified duration.

Within the flux time series I define a window that starts with the first data point and has a length of d_{win} points, where d_{win} must lie between the expected maximum number of points during a dip d_{max} and the length of the whole data set. This window will gradually slide through the data with an increment of n_{step} data points per step (compare Figure 3.1).

I want to compare the fluxes in the window with the median fluxes of its neighborhood. The neighborhood consists of the two surrounding sections, each of size d_{win}. If the current window happens to be near the boundaries of the time series, i.e. there is not enough room for a neighbor on one side of the window, I extend the neighborhood towards the center by doubling the size of the other neighbor. Alongside the median flux of the neighborhood m, I also compute its Median Absolute Deviation (MAD, Gauss 1816) to get an estimate of the data's dispersion. The MAD is more robust against outliers than the standard deviation and is defined as

$$MAD = \text{median}\left(\left|F^i_{\text{neighb}} - \text{median}(F_{\text{neighb}})\right|\right), \tag{3.1}$$

with F_{neighb} the flux data of the neighborhood. I define the flux threshold for a dip detection as $F_{\text{thresh}} = f_{\text{thresh}} \times m$ with the unit-less parameter f_{thresh}. However, if this value lies within $m \pm MAD$, I define the detection threshold as $F_{\text{thresh}} = m - MAD$ to make sure it lies in the detectable regime.

Next, I count the number of consecutive flux measurements in the window that fall short of F_{thresh}. To account for single upward outliers, a value above F_{thresh} is regarded as the end of the dip only if it is followed by a second datum of higher flux. If the duration of the low-flux event lies between the expected minimum and maximum dip durations d_{min} and d_{max}, the event is considered a dip detection.

After the window slid n_{step} data points further, the above steps are repeated until the end of the data set is reached. Figure 3.1 illustrates the principle of this technique on the example light curve of EPIC 220262993, the variable quasar discussed in Section 4.4.

[4]Barycentric Julian Day

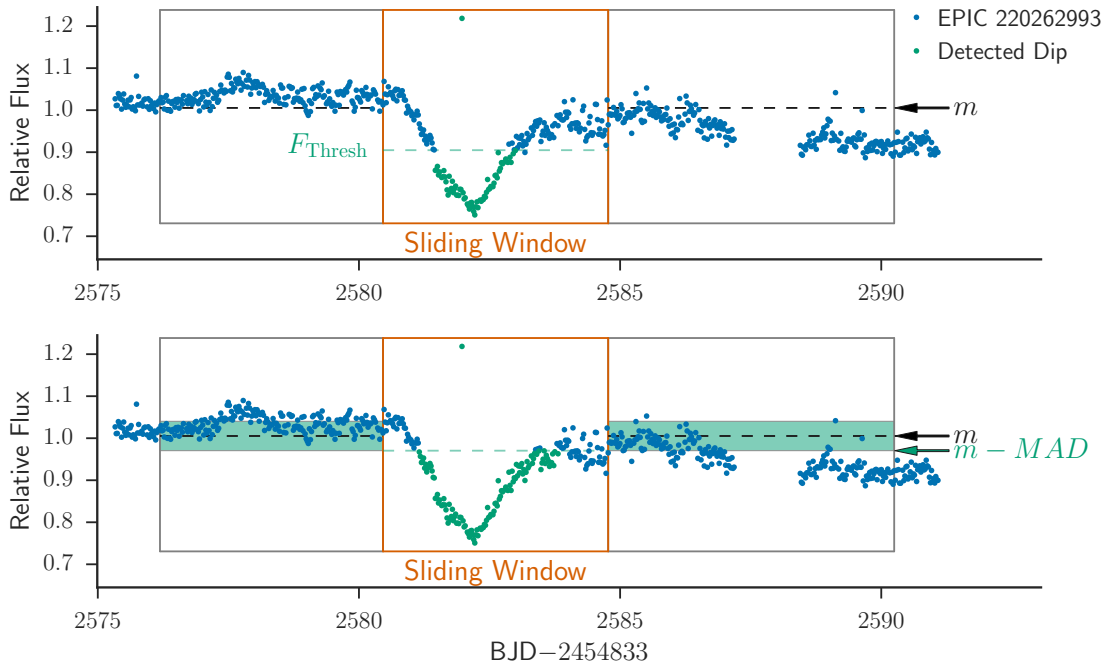

Figure 3.1.: Schematics of the Sliding Window technique. A section of the K2SFF photometry of EPIC 220262993 (blue circles) is scanned by the sliding window (orange rectangle) and its neighboring windows (gray rectangles) of size $d_{\mathrm{win}} = 200$ points, respectively. The detected dip (green circles) starts when the flux falls below a detection threshold, and ends with the first of two consecutive fluxes above the threshold. *Top:* The detection threshold is defined by F_{thresh}, the value of which is a fraction of the local median of the neighborhood m. *Bottom:* If, however, F_{thresh} lies within $m \pm MAD$ (green band), I use $m - MAD$ as the detection threshold to account for regimes of high dispersion.

3.1.3. Installation of `lcps`

`lcps` is made publicly available. It is listed on PyPI, its current version `0.4.dev` is tested on Python 2.7. The easiest way to install `lcps` is via pip[5]. The command

```
$ pip install lcps
```

in the terminal of a UNIX-based system will install `lcps` in the local Python path.

If the most current development version is preferred, it can be downloaded from `https://github.com/matiscke/lcps`. After unpacking the package, it is being installed by running the setup script

```
$ sudo python setup.py install
```

[5] `http://pypi.python.org/pypi/pip`

from the root directory of `lcps`. A full documentation of the package is available at http://lcps.readthedocs.org.

3.2. Determination of Effective Temperature

I developed an algorithm `TeffFit`, which fits observed multi-band photometry to template stars to obtain the effective temperature $T_{\rm eff}$ of an object. The interpolation between the templates is based on minimizing a chi-square statistic with a random walk Monte Carlo method.

3.2.1. Template Stars

Covey et al. (2007) assembled a matched stellar catalog from a high-quality subsample of 311652 point sources. The catalog is based on u, g, r, i, z magnitudes from the Sloan Digital Sky Survey (SDSS, Doi et al. 2010) and J, H, K_s magnitudes from the Two Micron All Sky Survey (2MASS, Skrutskie et al. 2006), where SDSS uses an AB-based photometric system and 2MASS uses a Vega-based system. Covey et al. estimated colors as a function of Morgan-Keenan (MK) spectral type by calculating synthetic colors ($u-g$, $g-r$, $r-i$, $i-z$, $z-J$, $J-H$, $H-K_s$) from flux-calibrated spectral standards assembled by Pickles (1998). These relations serve as my stellar model, with the spectral type converted to $T_{\rm eff}$ as follows: For dwarf stars (luminosity class V) from O9 to M6, I relate $T_{\rm eff}$ to a spectral type following Pecaut & Mamajek (2013, Table 5). For O5 dwarfs, I reduce the value in Vacca et al. (1996) by 1870 K, which is the average difference between the temperatures of Pecaut & Mamajek and Vacca et al. for O9 and B0 dwarfs. For red supergiants (luminosity class I) from K2 to M2, I use the relations in Levesque et al. (2005, Table 5). For red giants (luminosity class III) from F0 to K5, I take the values of Alonso et al. (1999). Later giants from M0 to M8 were taken from Perrin et al. (1998). From this, I obtain three separate color-temperature grids $c_{i,\,\rm model}(T_{\rm eff})$ for the luminosity classes I, III and V.

3.2.2. Temperature Sensitivity

A given color c_i has varying sensitivity on effective temperature depending on the temperature range. "Flat" colors that are not sensitive to $T_{\rm eff}$ in their respective range, i.e. $\partial c_i/\partial T_{\rm eff} \approx 0$, would add noise to the result without improving the fit. I obtain a rating of the sensitivity of a specific color by approximating the derivative $D(c_i) \equiv \partial c_i/\partial T_{\rm eff}$

with finite differences

$$D_1(c_i) \approx \frac{c_i(T_2) - c_i(T_1)}{T_2 - T_1}, \tag{3.2}$$

$$D_N(c_i) \approx \frac{c_i(T_N) - c_i(T_{N-1})}{T_N - T_{N-1}}, \tag{3.3}$$

$$D_n(c_i) \approx \frac{c_i(T_{n+1}) - c_i(T_{n-1})}{T_{n+1} - T_{n-1}}, \quad n \in \{2, ..., N-1\}, \tag{3.4}$$

where the T_n correspond to the discrete temperatures of the N model stars. While for the first and last model (Equation 3.2 and Equation 3.3) in the temperature range of each color c_i first-order approximations are used, we can perform a more accurate second-order approximation of central differences (Equation 3.4) for all models not at the boundary of the range. Figure 3.2 shows in its upper panel the temperature dependence $c_i(T_{\text{eff}})$ of luminosity class V models for all colors. All colors tend to become less sensitive to T_{eff} with increasing temperature, which is consistent with a simple black body model that describes a main-sequence star to first order. This trend is even more evident in the lower panel, where I show approximated derivatives $\partial c_i / \partial T_{\text{eff}}$ that correspond to these colors. For stars cooler than ∼A0V these derivatives show high fluctuation between different colors, while for earlier stars all colors become flatter than $1 \times 10^{-4}\,\text{mag}\,\text{K}^{-1}$. The temperature sensitivity is thus largely reduced in this spectral type range, increasing the uncertainty of the temperature fit. I addressed this problem by imposing a lower limit of $\partial c_i / \partial T_{\text{eff}}$, which is a compromise between improving the precision in the cold regime and avoiding an increase of ambiguity for hot objects. I found a value that serves both requirements and exclude a color c_i from further analysis if $D(c_i)$ falls short of $D(c_i)_{\text{min}} = 5 \times 10^{-6}\,\text{mag}\,\text{K}^{-1}$.

3.2.3. Goodness of Fit

I determine the effective temperature of an object by comparing its measured colors to the ones of each template star of a specific luminosity class. Treating the input color uncertainties as uncorrelated Gaussian noise, I measure the goodness of fit via a chi-squared approach. From the weighted sum of squared errors for n observables, Equation 2.8, I build the reduced chi-squared statistic dividing the sum by the number of degrees of freedom ν and obtain

$$\chi^2 = \frac{1}{\nu} \sum_{i=1}^{n} \frac{(c_i - c_{i,\,\text{model}})^2}{\sigma_{c_i}^2} \tag{3.5}$$

with c_i the observed colors, $c_{i,\,\text{model}}$ the model colors, and σ_{c_i} the statistical error of the latter. In the case of a single fitted parameter (T_{eff}), we have $\nu = n - 1$. The sum in Equation 3.5 is computed for every set of colors in the template table. Centered on the set with the smallest χ^2, I interpolate between the grid points, taking into account only the next two neighboring points, and obtain the cubic spline $\chi^2_{\text{interp}}(T_{\text{eff}})$. The effective

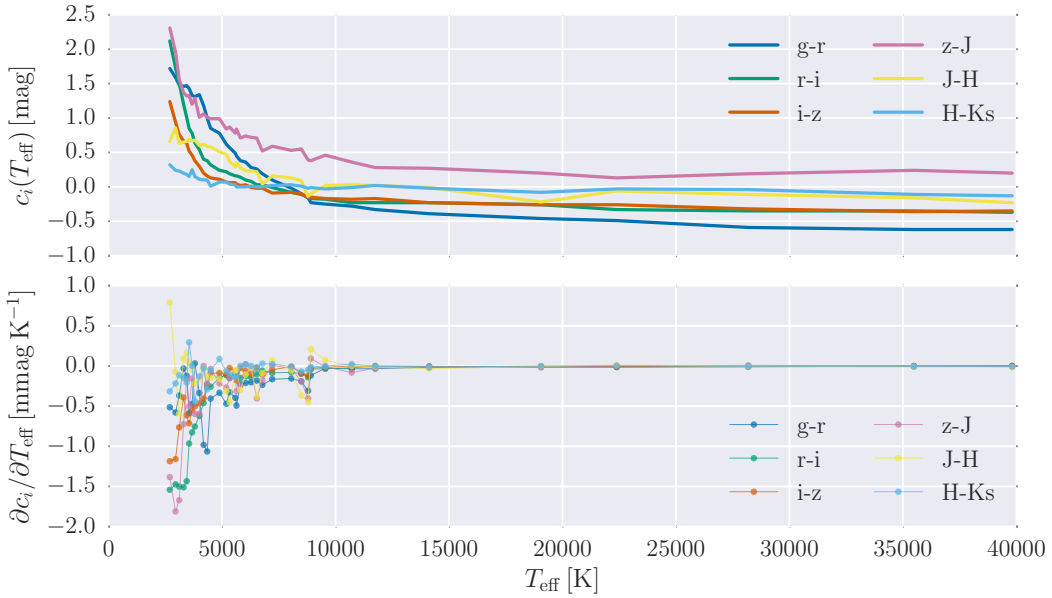

Figure 3.2.: Temperature sensitivity of the colors of luminosity class V model stars. *Top:* Temperature dependency of SDSS/2MASS colors. *Bottom:* Approximated derivative in temperature of the same colors.

temperature $T_{\rm min}$ at its minimum, $\chi^2_{\rm min}$, is kept as a result and stored together with this minimum.

3.2.4. Monte Carlo Sampling

I repeatedly generate noisy realizations of the data by sampling each color from a normal distribution centered on the actual measurement. The standard deviation of the Gaussian equals the error σ_{c_i} in this quantity. For each of these noisy versions of the measurement, I determine χ^2 and minimize it as described in Section 3.2.3. At first, a number of 30 such realizations are used to get a rough estimate of $T_{\rm eff}$. With this estimate, the temperature sensitivity $D(c_i(T_{\rm eff}))$ is computed and "flat" colors are excluded from further analysis (see Section 3.2.2).

After this selection, the actual Monte Carlo run begins: I choose the number of iterations $N_{\rm stat}$ high enough to account for statistical deviations. Validation tests of the `TeffFit` algorithm revealed that increasing $N_{\rm stat}$ to more than 100 entails a relative accuracy improvement of less than 0.01 while the computation time increases linearly with $N_{\rm stat}$. I search a compromise of accuracy and computational cost and choose $N_{\rm stat} = 200$ fits. To improve the quality of the fit, I limit the minimum chi-squared sum $\chi^2_{\rm min}$ to lie within a range of 0 to 10. The Monte Carlo loop stops after $N_{\rm stat}$ minima conform to this rule

or when the number of iterations exceeds $10\,N_{\mathrm{stat}}$. If the number of results $N_{\mathrm{min}} = N_{\mathrm{stat}}$, I assign the fit a *Quality Flag* $Q = AA$. If $1/3\,N_{\mathrm{stat}} \leq N_{\mathrm{min}} < N_{\mathrm{stat}}$, the fit is flagged with $Q = A$.

In the case of an even smaller number of results I employ a fallback level with less restrictive χ^2_{min} limits of -100 to 5000. A χ^2 sum of less than zero seems nonsensical when looking at its definition (Equation 3.5), but such a value can result from the spline interpolation of χ^2. Again I check for the number of successful fits and assign the fit a quality flag $Q = B$ if $N_{\mathrm{min}} = N_{\mathrm{stat}}$, and $Q = C$ otherwise. If instead no results at all were obtained, I drop all limits on valid χ^2_{min} values and assign any found minima a quality flag $Q = D$. In all cases I obtain a set of chi-squared minima and its associated temperatures.

In test runs of the algorithm, I often encountered spurious groups of minima at temperatures far off the main group of solutions. Since they compromise the accuracy and result only from oscillations in the interpolation step, I remove outliers that are farther away than two standard deviations from the mean temperature. Finally, I use `SciPy`'s[6] stats.norm.fit routine to fit a normalized Gaussian PDF

$$P = \frac{1}{\sqrt{2\pi\sigma^2}} \exp\left(-\frac{(T_{\mathrm{min}} - T_{\mathrm{eff}})^2}{2\sigma^2}\right) \tag{3.6}$$

to the histogram of the remaining data. This yields the determined effective temperature T_{eff} and its associated error σ.

Figure 3.3 shows a test run of `TeffFit`. I fed it with synthetic photometry corresponding to a star of luminosity class V with $T_{\mathrm{eff}} = 2951\,\mathrm{K}$. A consistent solution of 2930 K is recovered with a standard deviation of $\sigma = 80\,\mathrm{K}$.

3.2.5. Tests of the `TeffFit` Algorithm

Accuracy

To test the accuracy of the temperature fit, I aimed to compare its results with a set of reference objects. I used the same database of template stars that serve as the model grid for this. This would also reveal numerical issues near the grid points, e.g. oscillations in the interpolated chi-squared statistic. I employed an artificial error of $\sigma_c = 0.1$ for each color. Figure 3.4 shows the relative temperature deviation as a function of effective temperature for dwarfs. Only the template for an F0V star can not be recovered (crossed point). This is probably due to its flat $r - i$ color, which compromises the generation of synthetic errors for the fit. It can be seen that all other temperatures agree within 5 % for stars cooler than 8913 K and within 20 % for hotter stars.

[6] Scientific Computing Tools for Python (Jones et al. 2001–)

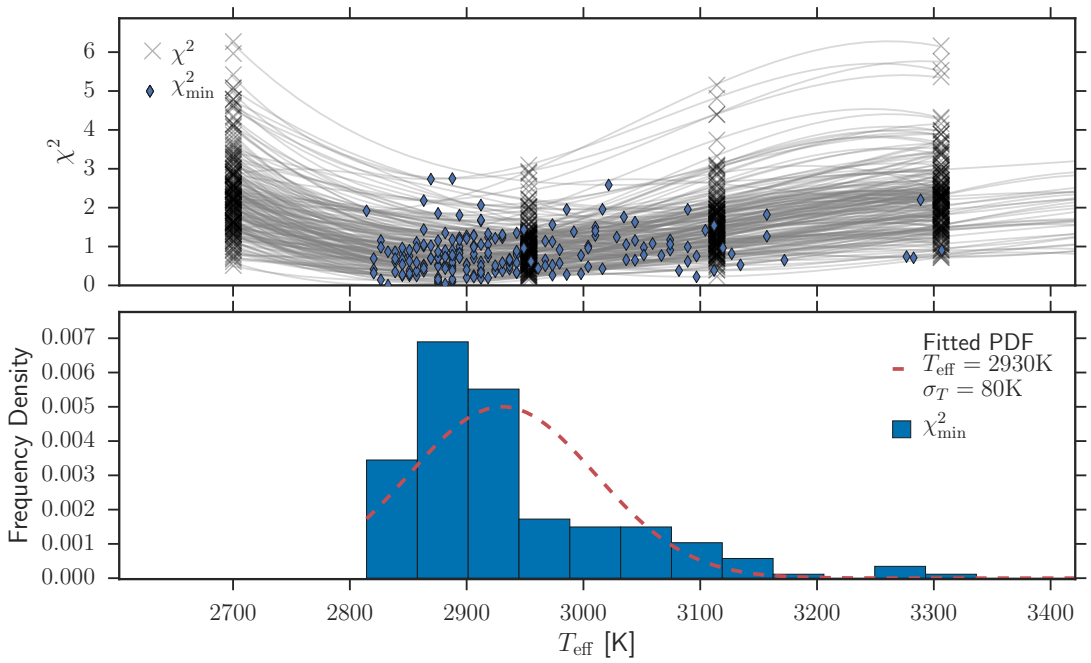

Figure 3.3.: `TeffFit` test run with 200 Monte Carlo iterations for luminosity class V. The algorithm was fed with synthetic colors from the model table that correspond to a M5V star with a temperature of 2951 K. *Top:* Goodness of fit results for several model entries (gray crosses) and interpolated χ^2 (gray lines). Blue diamonds indicate the minima of the interpolations. *Bottom:* Histogram of χ^2 minima. A Gaussian PDF (Red dashed line) is fit to the histogram to obtain the mean T_{eff} and standard deviation σ of the determined effective temperature.

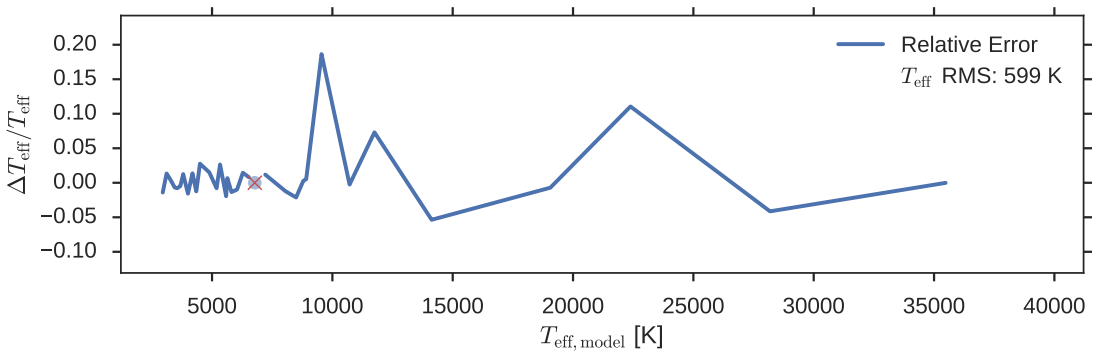

Figure 3.4.: Relative temperature deviation for luminosity class V. The plot shows the recovery of effective temperatures when `TeffFit` fits colors from its own template database. Temperatures are recovered within 20 % for all templates except for the F0V template, whose flat $r - i$ color compromises the error treatment.

SED Consistency Check

For a sample of objects, I compare their measured fluxes to a black body spectrum. Figure 3.5 shows *grizJHK* fluxes and corresponding black body spectral energy distribution (SED) for a star of luminosity class I, III, and V, respectively. Blue points are fluxes simultaneously measured with the Gamma-Ray Burst Optical/Near-Infrared Detector (GROND, Greiner et al. 2008), given in the AB system with their photometric uncertainties. The green curve in each plot is a synthetic spectrum of a black body with a temperature T_{eff} that resulted from the temperature fit of the observed object. The giant and supergiant examples show significant red excess, possibly related to the CO molecular band that resides at 2.29 µm in the K_s band (Ivanov et al. 2004). Nevertheless, the positions of peak wavelengths in the black body and measured spectra agree well, certifying `TeffFit` a good recovery of a star's *Wien temperature* (Wien 1896).

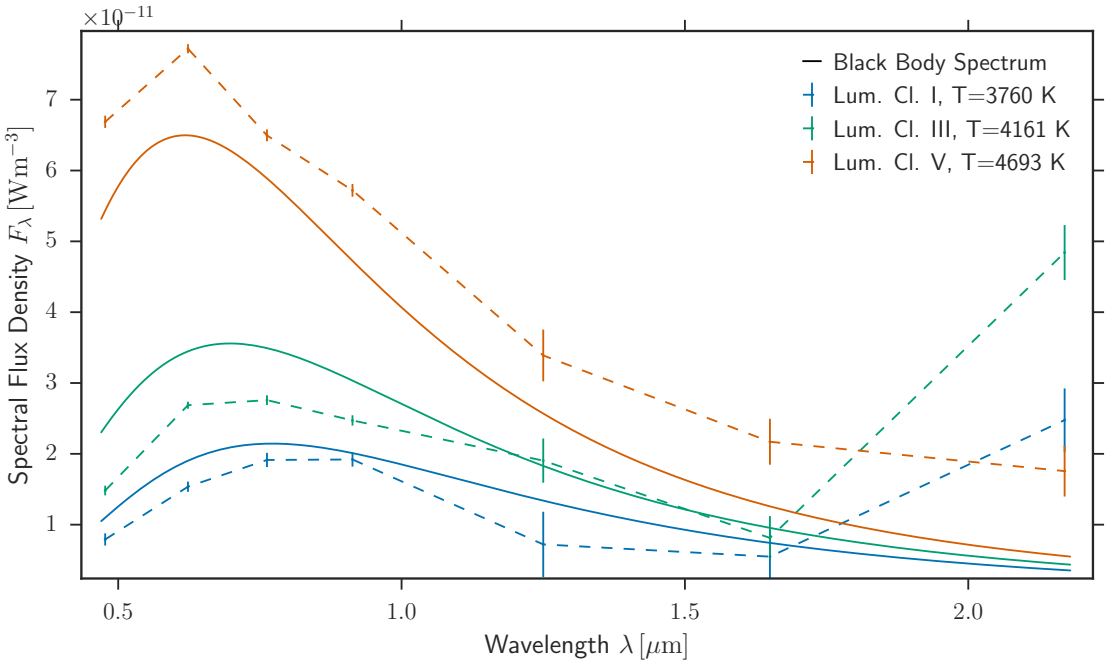

Figure 3.5.: Flux-calibrated photometry compared to black body SEDs. Dashed lines with error bars are observed *grizJHK* fluxes in the AB photometric system. For each of these measurements I determine the effective temperature with `TeffFit` and plot a generic black body spectrum of the corresponding temperature (solid line of same color). The three arbitrarily picked targets were classified as follows: blue: luminosity class I, $T_{\mathrm{eff}} = 3760\,\mathrm{K}$. Green: luminosity class III, $T_{\mathrm{eff}} = 4161\,\mathrm{K}$. Orange: luminosity class V, $T_{\mathrm{eff}} = 4693\,\mathrm{K}$.

Comparison with Theoretical Models

I compared the results of `TeffFit` to temperatures derived from theoretical models and/or spectral analysis for a small number of arbitrarily chosen objects (see Table 3.1). For each of these objects, I listed T_{eff} from the EPIC stellar classification catalog and

used the VOSA[7] tool to fit an ATLAS9 model atmosphere (Castelli & Kurucz 2004) to the photometry listed on ExoFOP[8]. From the same photometry, `TeffFit` yielded the temperatures listed in the last column for main-sequence stars. The values in the "SpecMatch" column are the result of a spectral analysis with a stellar parameter extraction technique by Petigura (2015) and were posted to ExoFOP by Ian Crossfield. The table also lists data for my planetary candidate, EPIC 217393088. For this target, `TeffFit` agrees well with the result from the ATLAS9 SED fit. The temperature listed in the EPIC is about 500 K higher. For a possible explanation of this discrepancy, see Section 4.3.5. Unfortunately, there are no spectra available for this object.

Target	Effective Temperature [K]			
EPIC ID	ATLAS9	EPIC [a]	SpecMatch[b]	`TeffFit` [c]
201384232	$4750 \pm 125^{\dagger}$	5370 ± 255	5767 ± 58	5745 ± 210
201403446	6250 ± 125	6409 ± 104	6256 ± 37	6159 ± 514
201295312	$7750 \pm 125^{\dagger}$	5535 ± 133	5912 ± 51	5590 ± 170
217393088	5500 ± 150	5981 ± 176	–	5449 ± 42

[a] Stellar classification of the EPIC catalog (Huber et al. 2016)
[b] As listed on ExoFOP by Ian Crossfield on 2016-06-28
[c] Assuming luminosity class V
[†] Bad fit ($\chi^2 > 10^2$)

Table 3.1.: Comparison of temperature fits from different sources for several EPIC targets. The results from theoretical model fits (ATLAS9, Castelli & Kurucz 2004) are compared with $T_{\rm eff}$ from the EPIC, from a spectral analysis using SpecMatch, and `TeffFit` temperatures. I also list the results for my planetary candidate, EPIC 217393088.

3.3. Distance and Extinction Estimate

It extended `TeffFit` to constrain the distance to stars and the extinction along the line of sight by fitting simultaneously for these parameters and the stellar effective temperature. For a given object, I query the IRSA DUST[9] service for galactic dust reddening in the line of sight to obtain the color excess E_{B-V}, which is related to the observed and intrinsic $B-V$ color by

$$E_{B-V} = (B-V)_{\rm observed} - (B-V)_{\rm intrinsic}. \tag{3.7}$$

Following Schlafly & Finkbeiner (2011), the maximum of the visual extinction A_V is given by $A_V^{\rm max} = 3.08 \times E_{B-V}$. This value represents the full reddening within the Milky Way along the line of sight. I impose 7 fractions of $A_V \in \{0, \ldots, A_V^{\rm max}\}$ to account for different amounts of Galactic extinction. A finer grid would only be reasonable for photometry of very high precision. Next, I convert A_V to the extinction in SDSS/2MASS bands

[7] VO SED Analyzer, http://svo2.cab.inta-csic.es/theory/vosa/
[8] Exoplanet Follow-up Observing Program, https://exofop.ipac.caltech.edu
[9] Galactic Dust Reddening and Extinction, http://irsa.ipac.caltech.edu/applications/DUST/

A_x and subtract these values from the measured magnitudes m_x to de-redden an object. `TeffFit` is then run for all luminosity classes, which makes for $7 \times 3 = 21$ combinations of extinction and luminosity class. For each of these realizations, I compute the logarithmic distance

$$\log d = 1 + \frac{\mu}{5} \tag{3.8}$$

with the distance modulus $\mu = m_J - M_J$. To obtain the absolute magnitude M_J, I interpolate between the values given in Pickles (1998), which were transformed using the relations derived by Carpenter (2001). From these 21 sets of parameters, I keep the one that yields the lowest χ^2_{avg}, which is the mean of χ^2_{min} (compare Section 3.2.4). To visualize the distribution of realizations in A_V and T_{eff}, I imposed an evenly spaced grid of 1000 A_V fractions and performed the procedure described above for luminosity classes I, III and V on an arbitrary GROND observation. Figure 3.6 shows the distribution with a clear clustering among the luminosity classes superimposed by a χ^2_{avg} heatmap, which I reconstructed from the results by interpolating on a triangular grid between the points. The trend of higher effective temperatures for larger extinction is expected from Galactic extinction models (Bailer-Jones 2011). In this case, a star with $T_{\mathrm{eff}} = (3972 \pm 29)\,\mathrm{K}$ and $A_V = 0.22\,\mathrm{mag}$ yields the best fit with $\chi^2_{\mathrm{avg}} = 0.95$.

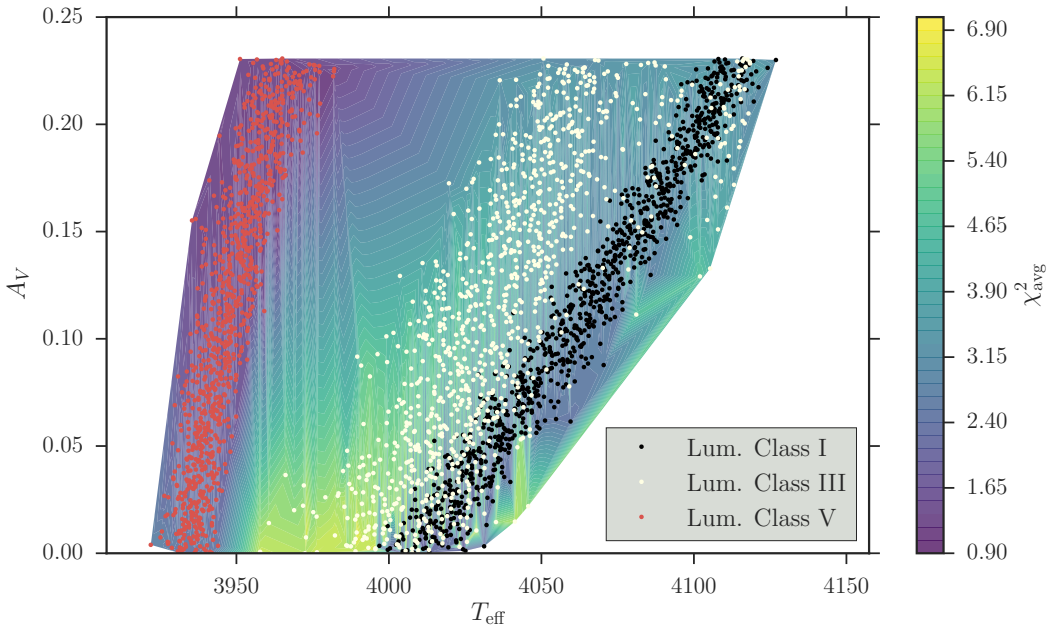

Figure 3.6.: χ^2 map of 3000 runs of `TeffFit` with varying A_V. I run the fit for a single object with 1000 evenly spaced fractions of A_V for each luminosity class, respectively. The color scale shows the average χ^2 of a run, which I interpolate on a triangular grid between the points. The clustering of the three different luminosity classes can clearly be seen. The best match ($\chi^2_{\mathrm{avg}} = 0.95$) for this object is a K7V star with $T_{\mathrm{eff}} = (3972 \pm 29)\,\mathrm{K}$ and $A_V = 0.22\,\mathrm{mag}$. This is almost the maximum extinction $A_V^{\mathrm{max}} = 0.23\,\mathrm{mag}$ along this line of sight.

Figure 3.7 shows a preliminary estimate of distance d and interstellar reddening A_V by this procedure for 1058 stars observed with GROND. These stars remained in the sample after saturated sources were removed. Since the observation was a very deep exposure, the sample contains mainly stars of faint apparent brightness, consistent with the large inferred distances and extinction estimates in the plot.

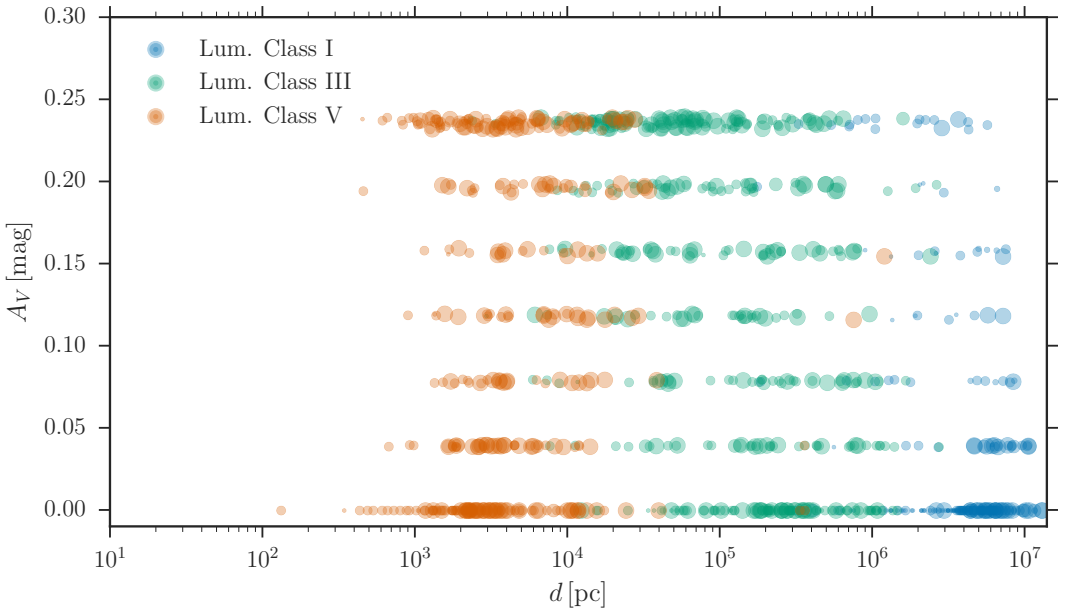

Figure 3.7.: Extinction versus distance for a set of 1058 target stars. For each object, I perform de-reddening with seven different fractions of Av and run `TeffFit` for each of three assumed luminosity classes. Of these 21 combinations, the result with the lowest mean χ^2_{min} is kept and depicted in the plot. The quality of the fit (compare Section 3.2) is reflected by the size of the point, with larger points meaning better quality.

The technique described in this section is an ongoing effort. First tests show a reasonable relative distribution of objects for the applied luminosity classes in terms of distance, effective temperature, and interstellar reddening (see Figure 3.6 and Figure 3.7). However, the inferred distances will have to be tested against predictions from Galactic population models and distances determined by other methods.

3.4. Outlook

`lcps` is generally compatible with any time series data and is ready to be used on photometry of future exoplanet detection surveys such as TESS or PLATO. It was tested with *Kepler* long cadence light curves and yielded the first results.

`TeffFit` is software under development. The tests described above show that it succeeds in constraining the effective temperature of a star of known luminosity class with adequate accuracy. Temperature uncertainties, which are inferred from the histogram of χ^2 minima (see Figure 3.3), have yet to be tested for consistency by a cross-check with representative photometry. In its current version, the tool lacks the capability of reliable distance determination and distinction of luminosity classes from photometry alone. Ongoing work seeks to achieve a simultaneous inference of distance and Galactic extinction without additional observables of a target. A future version could automatically distinguish between luminosity classes, e.g. by the approach described by Huber et al. (2016), who distinguish between giants and dwarfs based on analytical functions of T_{eff} and $\log(g)$.

4. Results

In this chapter, I describe the path from selecting the sample of targets, to the investigation of the selected objects, to deeper inspection of interesting candidates. I show how I constrained orbital parameters for a serendipitously discovered exoplanet, a candidate hot Jupiter around a main-sequence star in Section 4.3. Finally, I outline the observation and analysis of a quasar subject to aperiodic dipping events in Section 4.4.

4.1. Selecting the Targets

Since the approach of visual inspection consumes a lot of time, it is appropriate to focus only on targets where the detection of such an event is feasible. Depending on the K2 Campaign, I applied one of two different methods to reduce the set of K2 targets to a manageable number of promising objects.

4.1.1. Conditions on Host Star Colors

In the K2 Campaigns 3 to 6, I imposed conditions on the target stars to focus my search on late-type dwarfs of mainly class M. These stars are particularly favorable for several reasons: Their comparatively small size leads to a larger signal in a transit event, i.e. a higher planet-to-star ratio $R_\mathrm{p}/R_\star$ for planetary transits (Howard et al. 2012). The stronger signature extends the range of detectable transiting bodies towards smaller sizes. According to statistical studies that focused on M dwarfs observed by *Kepler* (Dressing & Charbonneau 2013), planets exist nearly around all class M dwarf stars. These targets have yielded a disproportionate number of multiplanet systems and potentially habitable planets (inferred from their irradiation level similar to the Earth's, Mann et al. 2013). Restricting to class M stars leaves a sufficient number of targets, since $\sim 70\,\%$ of all stars are M dwarfs (Bochanski & Claire 2010).

In order to obtain a list of only late-type stars, I applied conservative constraints on the 2MASS colors to the initial set of objects. A star is kept in the target list if

$$J - H \geq 0.55 \quad \text{and} \tag{4.1}$$

$$H - K \geq 0.1 \tag{4.2}$$

with J, H, and K the 2MASS magnitudes of the star. With these criteria, I ended up with a few thousand targets per K2 Campaign (see Table 4.1).

4.1.2. Conditions on Light Curve Shapes

In Campaigns 7 and 8, I selected targets based on the shape of their light curve prior to visual inspection. The Sliding Window technique described in Section 3.1 is particularly useful in the search for deep and long-lasting dips similar to the examples presented in Section 2.5. I used `lcps` to search for such signatures in the long cadence photometry of K2 Campaigns 7 and 8. To do so, I allowed only dip lengths of $d_{\mathrm{min}} = 30$ points to $d_{\mathrm{max}} = 199$ points within a 200 point window, corresponding to dip durations of 14.7 h to 97.6 h. The upper limit d_{max} mitigated false detections resulting from long-term trends in the time series. I chose the flux threshold for each run individually such that I reduced the targets to a manageable number while discarding as few potentially interesting light curves as possible. The limited number of targets after the pre-selection made restraints on host star colors, as described in Section 4.1.1, superfluous.

I applied the pre-selection both on the standard *Kepler* pipeline photometry and on the K2SFF product of Vanderburg & Johnson (2014) (compare Section 2.4.1). For each given Campaign, I investigated first the photometry from the pipeline, which is released several weeks earlier than its K2SFF counterpart. When the latter was released, I used only K2SFF data as its better photometric precision allows to search for shallower dips in the data (see Table 4.1) and I adapted the threshold flux factor f_{thresh} accordingly.

		`lcps` Input parameters					Number of targets		
C	HLSP	d_{win}	n_{step}	d_{min}	d_{max}	f_{thresh}	initial	selected	inspected
3	K2SFF	–	–	–	–	–	16834	7138	252
4	K2SFF	–	–	–	–	–	17203	7920	340
5	K2SFF	–	–	–	–	–	25775	8054	7
6	K2SFF	–	–	–	–	–	28290	8384	50
7	PDC	200	10	30	199	0.95	13469	275	275
7	K2SFF	200	10	30	199	0.98	13469	422	137
8	PDC	200	10	30	199	0.9	24187	141	141
8	K2SFF	200	10	30	199	0.95	24187	266	82

Table 4.1.: Pre-selection of targets for K2 Campaigns C3 to C8. The window size d_{win}, the step increment n_{step}, and the minimum and maximum dip durations d_{min} and d_{max} are given in number of data points, respectively. f_{thresh} is the fraction of the local median flux m, below which a dip is detected. The actual detection threshold can be lower in noisy regions of the data (see Section 3.1.2). Light curves from C3 to C6 were not processed by `lcps` but pre-selected based on color criteria (see Section 4.1.1).

In the pre-selection of Campaign 7, I manually discarded the light curves of EPIC 200061226 – 200062827. These 1602 datasets belong to large tiled regions that cover the paths of the dwarf planet Pluto and the Trojan and Hilda asteroids, as well as the open cluster Ruprecht 147[1].

[1] see K2 programs GO7012, GO7025, and GO7035; http://keplerscience.arc.nasa.gov/k2-approved-programs.html

The PDC photometry of Campaign 8 shows strong systematics on timescales similar to the dip durations I looked for. I mitigated large numbers of erroneous detections by lowering the threshold factor for this Campaign to $f_{\mathrm{thresh}} = 0.9$.

4.2. Investigation of Light Curves

For each selected target, I performed a visual inspection of the K2SFF light curve extracted with the default "best" photometric aperture (compare Figure B.2). After a cross-match of our sample with the corresponding coordinates in the K2 target list, I queried the 2MASS All-Sky Catalog of Point Sources (Skrutskie et al. 2006) via the Vizier[2] service. These photometric data can be used to infer the spectral type of a candidate's host star using the `TeffFit` tool (see Section 3.2). For Campaigns 3 – 6, I also used the obtained magnitudes to constrain the list of targets for visual inspection to late-type stars (see Section 4.1).

To speed up the investigation routine, I applied a custom Python script that performs all additional steps other than the actual eyeballing. On start-up, it creates a target list for the investigation session. It contains either all targets of a Campaign that obey the color criteria in Equation 4.1 or the results from a light curve pre-selection (Section 4.1.2). Objects that have already been investigated are discarded. For every object in the target list, the script parses the light curve file to the `TOPCAT`[3] software where one can investigate the light curve in a plot of corrected flux vs. BJD. Upon exiting `TOPCAT`, the script provides a prompt where a set of evaluation flags can be typed in. The flags are then stored in a notes file together with the EPIC number of the target for a potential follow-up investigation.

I performed visual inspection on 649 of 31496 color-selected targets from K2 Campaigns 3 – 6, and on 635 of 1104 targets selected by `lcps` from Campaigns 7 and 8 (compare Table 4.1). The main bulk of the color-selected light curves are essentially flat or show only low-frequency features related to spacecraft induced systematics. However, I have rediscovered a number of planetary candidates and confirmed planets, as well as EB systems and stars with spot-induced variations. With the deployment of `lcps` from Campaign 7 on, the flat and slowly varying light curves disappeared from the target list. Now, all of the pre-selected objects had some sort of dimming event in their photometry, with the majority associated to systematic errors or intrinsic stellar variability. A large fraction of targets showed clear indicators of EB systems; I did not further investigate them.

[2] `http://vizier.u-strasbg.fr/`
[3] Tool for OPerations on Catalogues And Tables by Taylor (2005)

4.3. EPIC 217393088.01: A New Planetary Candidate

I identified a possible transit signature of a planetary companion in the light curve of EPIC 217393088. This object was observed in Campaign 7 in long cadence mode at coordinates (J2000) RA = 19 h 17 m 45.39 s, Dec = −20 h 39 m 15.75 s. It has a Kepler magnitude of $K_p = 15.293$ mag and is listed in the 2MASS catalog under the alias 2MASS J19174538-2039156 with

$$J - H = \quad 0.314 \pm 0.042 \tag{4.3}$$
$$H - K = -0.006 \pm 0.058 \tag{4.4}$$

and thus does not meet the color criteria I applied for earlier Campaigns (compare Equation 4.1). It was not selected by `lcps` either, since I tuned the parameters in Table 4.1 to search for deep and extended dips.

I encountered EPIC 217393088's light curve during a test run of my inspection script on May 18, 2016. It was included in a sample of 51 targets that were randomly chosen without conditions on their photometric color or on the shape of their light curve. The target is not listed as a planetary candidate or Kepler Object of Interest (KOI) on the NASA Exoplanet Archive (as of December 10, 2016), so I evaluated the planetary origin of the transit signal and determined planetary and orbital parameters of this candidate.

4.3.1. K2 Light Curve

The K2SFF light curve of EPIC 217393088 shows numerous periodic dips in flux of $\sim 1\,\%$ depth (see top panel of Figure 4.1). The signal is also present in the PDC data, and an investigation of the target pixel file revealed no conspicuous features that one might correlate to a false positive scenario.

The processed photometry still contains significant low-frequency variations. Thus, I detrended the time series by repeatedly removing outliers and applying a running median filter to the data. The reason for choosing this technique is its better preservation of shape and features of the signal compared to other approaches such as moving average or a Savitzky–Golay filter (Savitzky & Golay 1964). The data are at first cleaned from upward outlier points which, if kept, would affect the detrending and impair the accuracy of our transit analysis. Large positive excursions from the bulk light curve are usually caused by cosmic rays hitting the detector or asteroids passing through the photometric aperture (Vanderburg et al. 2015b). I excluded points that are farther than a standard deviation from the mean and then applied a running median filter without these outliers. I implemented the filter as follows: For each flux measurement F_i, I computed the median m of the fluxes in a range $[i - N/2,\, i + N/2]$, where N is the bin size. The new flux value is $F_{i,\mathrm{new}} = F_i/m$. The bin was then shifted by one data point, $i \to i+1$, and the previous steps were repeated. Through trial and error, I found that a bin size of $N = 31$ allowed

a robust removal of the systematic variations while safely preserving the shape of the transits.

The outlier removal and filtering are repeated for two iterations (see Figure 4.1). Through detrending, the out-of-transit RMS deviation decreased from $\sigma_{\mathrm{rms}} = 8500\,\mathrm{ppm}$ to $\sigma_{\mathrm{rms}} = 730\,\mathrm{ppm}$. Following the definition of Kovács et al. (2002), the mean relative transit depth of $\bar{\delta} = 0.012$ implies a signal with $SNR = \delta/\sigma_{\mathrm{rms}} \approx 16$ in the detrended light curve.

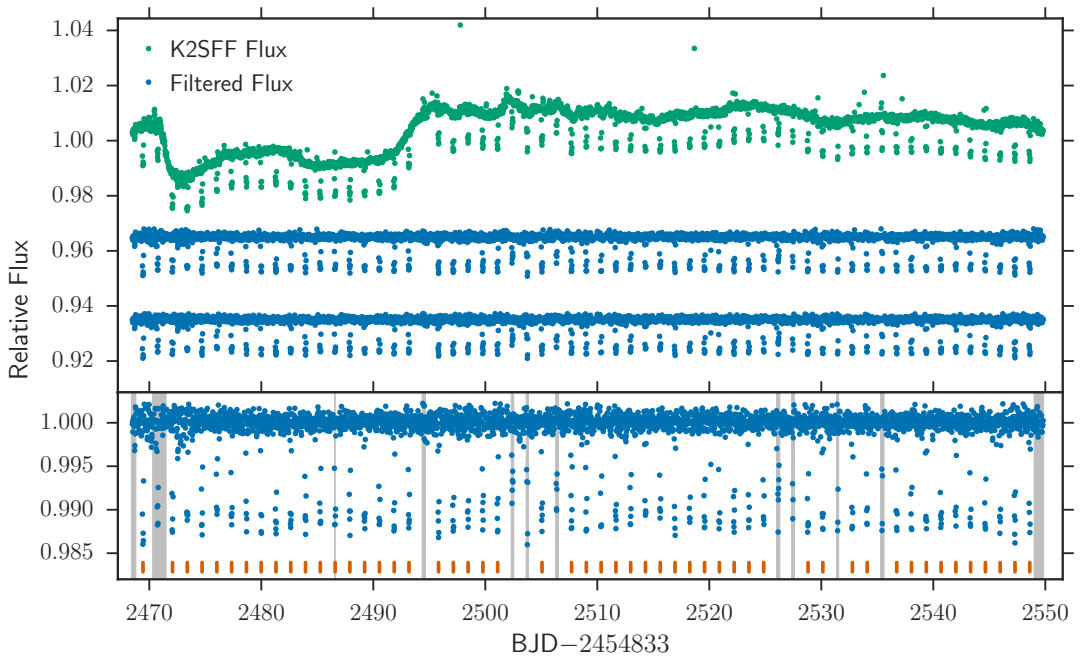

Figure 4.1.: Detrending of EPIC 217393088 photometry. *Top:* Original K2SFF data (green, some extreme outliers not shown) and data between iterations of outlier-removal and detrending (blue), offset for clarity. In each step, upward outliers farther than one standard deviation from the mean were removed and a running median filter was applied. *Bottom:* Detrended light curve. I removed regions with prominent artifacts from further analysis (shaded areas). The 52 uncorrupted transits are located at the orange markers and clearly visible by eye.

The bottom frame of Figure 4.1 shows the K2SFF light curve after detrending. Some regions show remaining trends or significant artifacts that were existent in the original data. I excluded these parts from further analysis to prevent losses of accuracy of our fit (grayed out areas in the figure). After this vetting step, I recognized 52 remaining transit signatures in the data set (orange markers).

4.3.2. Periodicity

For the following analysis, a precise measurement of the orbital period is vital. Classical spectral tools such as the Fourier transform (for evenly spaced data) or the Lomb-Scargle Periodogram (for unevenly spaced data; see Lomb 1976) are hardly suitable, because they are based on variations of sinusoidal shape (Feigelson & Babu 2012). Kovács et al. (2002) introduced a Box Least Squares (BLS) technique, which models the time series as an alternation between two discrete levels, i.e. a box-shaped signal. It considers a set of trial periods and folds the data about each of these periods. After a binning step, a least squares fit is performed and the spectral power is determined from the relative amplitude of the low-level state.

I determined the period of the signal in the detrended light curve with a BLS periodogram using the implementation of the NASA Exoplanet Archive (Akeson et al. 2013). With a fixed period step size of $\Delta P = 2 \times 10^{-4}$ d and a bin size of 6.3 h, I obtained the periodogram shown in Figure 4.2. It reveals a distinctive peak at $P \approx 1.32$ d and its harmonic frequencies. There is another signal around ~ 0.062 d $= 1.49$ h without a corresponding entry in the list of known spurious frequencies (Christiansen 2013). I suspect this is a higher harmonic of remaining systematics due to thruster burns of the spacecraft, which occur roughly every six hours (Scaringi et al. 2016). To fine-tune the period, I ran the algorithm again with a narrow range of test periods of 1.27 d to 1.37 d and a step size of $\Delta P = 5 \times 10^{-5}$ d. The resulting periodogram (see right panel of Figure 4.2) resembles a sinc function, which is the Fourier transform of a box-shaped signal. This narrowed down the period to $P = (1.3195 \pm 0.0048)$ d, giving the half width at half maximum (HWHM) of the peak as the uncertainty.

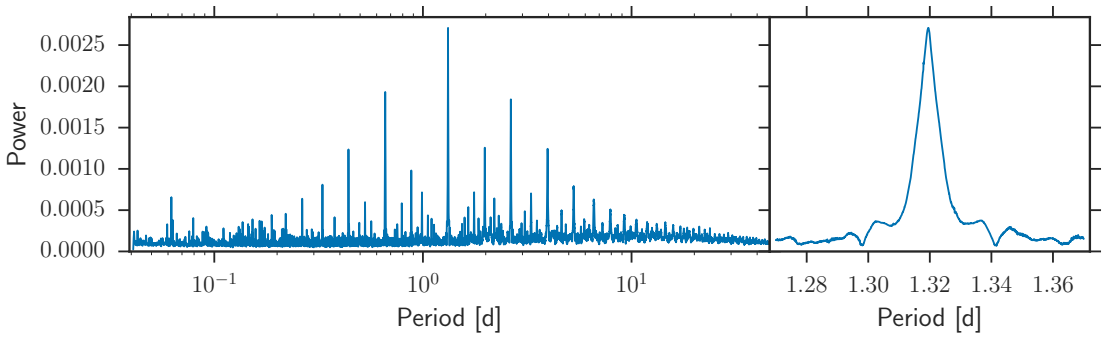

Figure 4.2.: BLS periodogram of the detrended light curve of EPIC 217393088. *Left:* Full periodogram ranging from 0.04 d to 80 d. The peak with the highest power corresponds to the transit signal at $P \approx 1.32$ d. Other prominent peaks with multiples of this period can be identified as harmonics of the transit period. There is another signal apparent around ~ 0.062 d with no corresponding entry in the list of known spurious frequencies (Christiansen 2013). *Right:* High-resolution periodogram about the transit period. This signal results from a second BLS run with a narrow range of test periods of 1.27 d to 1.37 d. It allows a fine-tuning of the orbital period to $P = (1.3195 \pm 0.0048)$ d.

Each transit lasts only about three hours. With *Kepler*'s integration time of 29.424 min in long cadence mode, there is significant smearing that distorts the transit signal and leads to poor sampling of single transits. To compensate for this effect, I assume that the system's geometry does not change between two transit events and *phase-fold* the time series about the orbital period P. Using the phase

$$\Phi = \frac{t - t_0}{P} - N_{\mathrm{orb}} \tag{4.5}$$

with orbit number N_{orb} instead of the original time data t as the time axis, I cover all parts of the folded transit with a high sampling rate. I fixed t_0 to the first time of inferior conjunction in the data set. The top panel of Figure 4.3 shows the phase-folded light curve color-coded by absolute time of the original data. The color-coding helps to spot temporary features that are poorly resolved with *Kepler*'s cadence, such as spot-crossing events. Indeed, one can see a delayed start of the dimming for a few transits early in the light curve. This could in principle be explained by an additional massive body in the system. However, a planet with such a short period is expected to experience strong tidal forces that cause a transfer of orbital angular momentum to the stellar spin (Maciejewski et al. 2016). This orbital decay quickly destroys a potential mean-motion resonance necessary to produce detectable TTVs. I therefore exclude TTVs as the cause for the delayed ingress. It can be explained by a stellar spot that was occulted by the planet during ingress. However, the light curve shows an overall lower quality before BJD $- 2454833 \approx 2476$, making the feature likely a spurious deviation.

The phase-folded light curve appears to have a slight bulge surrounding the transit signal. This detail is not visible when folding the PDC data, I therefore attribute this to systematics of the detrending routine.

4.3.3. Light Curve Model and Stellar Limb Darkening

Accurate light curve models can be fit to transit events to constrain stellar and planetary parameters (Hubbard et al. 2001). To first order, the course of the light curve during the transit depends on the stellar and planetary radii and on the projected trajectory of the planet. However, the shape of the resulting dip is significantly altered by stellar limb darkening, which causes a dimmer image near the edge of the stellar disk. Thus, limb darkening has to be taken into account to compute accurate transit models. The complexity of this calculation is largely dominated by the assumed stellar intensity profile. Several functional forms have been used, including linear (Schwarzschild & Villiger 1906), quadratic (Kopal 1950), square-root (Diaz-Cordoves & Gimenez 1992), logarithmic (Klinglesmith & Sobieski 1970), exponential (Claret & Hauschildt 2003), and four-parameter nonlinear laws (Claret 2000). Some of these profiles do not have analytic solutions. In these cases, one obtains the missing flux δ caused by a transiting planet by integrating the projected intensity I over the area masked by the disk of the planet S, i.e.

$$\delta = \int_S I \, \mathrm{d}S. \tag{4.6}$$

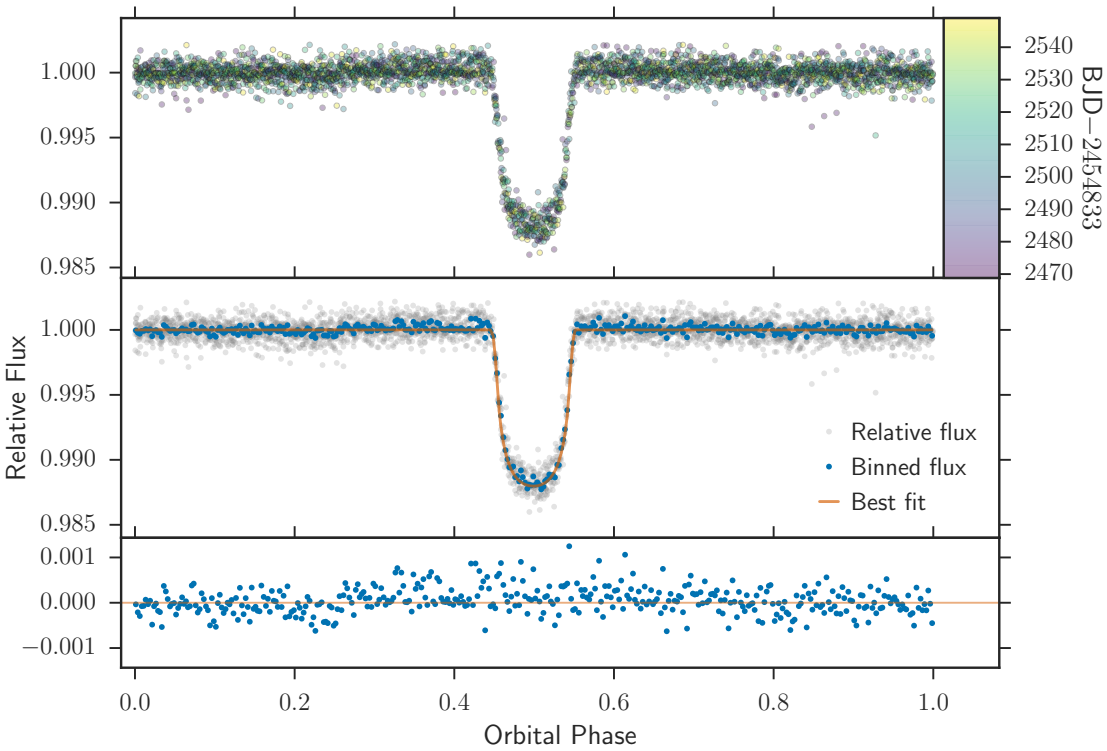

Figure 4.3.: Phase-folded light curve and transit fit of EPIC 217393088. *Top:* The detrended time series are folded about the transit period and color-coded by absolute time. *Middle:* Phase-folded photometry (gray points) is placed into bins of 4.75 min width (blue points). I fit a transit model to the binned data and show the best-fit model in orange. *Bottom:* Residuals of the transit fit with an deviation of 2.9×10^{-4}.

This can be computationally expensive if high accuracy is needed (Kreidberg 2015). The `batman`[4] package provides efficient computation of transit light curves for any of the mentioned radially symmetric limb darkening laws. I used the software to obtain the models I needed for the following transit analysis.

Since there is no reliable source of theoretical limb darkening coefficients for EPIC 217393088, I fit them in the transit-fitting procedure (see Section 4.3.4). The optimal choice of a limb darkening law for this purpose depends largely on its behavior on accuracy and precision in the retrieval of transit parameters. In this context, Espinoza & Jordán (2016) studied the bias-variance trade-off in the *Kepler* bandpass for $R_\mathrm{p}/R_\star$, $a/R_\star$, and i using a metric based on the mean-squared error

$$\mathrm{MSE} = \mathrm{Bias}(\theta_i)^2 + \mathrm{Var}(\theta_i) \tag{4.7}$$

and light curves from the `batman` package. The performance of the compared limb darkening laws shows a strong dependence on the light curve noise level. Since the authors

[4]BAsic Transit Model cAlculatioN in Python (Kreidberg 2015)

made their analysis code available[5], I used it to compare the performance of the different laws in the parameter regime of my transit signal, i.e. with $P \approx 1.3\,\mathrm{d}$, $R_\mathrm{p}/R_\star \approx 0.09$, $a/R_\star \approx 3$, $i \approx 89.1°$, and a light curve precision of 730 ppm. These first-guess values were obtained from a simplified transit fit on the phase-folded light curve of EPIC 217393088. I adopted stellar parameters of the target from the EPIC (compare Table 3.1). I did not consider an exponential law, since its negative intensity values near the outermost regions of a stellar disk prove it to be fundamentally non-physical (Espinoza & Jordán 2016). Consistent with the findings of Espinoza & Jordán (see their Figure 7), there is few difference in MSE between the laws in this noise level regime. I therefore opted for the widely used quadratic law

$$I(\mu) = I_0(1 - u_0(1-\mu) - u_1(1-\mu)^2), \tag{4.8}$$

with the intensity at the center of the disk I_0, the normalized radial coordinate μ, and the limb darkening parameters u_0 and u_1, due to the compact prior volume (Kipping 2013a) and to facilitate comparison.

4.3.4. Planetary Parameter Estimation

To determine credible regions for selected planetary parameters of EPIC 217393088.01, I performed an MCMC analysis and obtained a joint a-posteriori probability distribution (hereinafter also referred to as "posterior") of $R_\mathrm{p}/R_\star$, u_0, u_1, t_0, $a/R_\star$, i, e, and ω. The phase-folded light curve was placed into bins of $0.0025 \times P = 4.75\,\mathrm{min}$ width, and transit models as described in Section 4.3.3 were fit to the binned data. The orbital period of the planet is known from the BLS periodogram with high accuracy, thus I fixed P to the value determined in Section 4.3.2.

Orbital Eccentricity

In a transit fit, the eccentricity of the orbit typically shows a strong covariance with other parameters. In the following, I will justify my assumption of a circular orbit, $e = 0$, for EPIC 217393088.01. I performed a first fit in which I treated e and the argument of periastron as free parameters. I adopted a uniform prior for ω, since there should be no preferred orientation of exoplanet orbits in space. In contrast, there is evidence for a non-uniform distribution of eccentricities, largely due to tidal circularization (Trilling 2000). As advocated in Kipping (2013b), the Beta distribution

$$P(e, \alpha, \beta) = (1-e)^{\beta-1} e^{\alpha-1} \frac{\Gamma(\alpha+\beta)}{\Gamma(\alpha)\Gamma(\beta)}, \tag{4.9}$$

here expressed in terms of Gamma functions, provides a good match to the currently observed distribution of e. Kipping proposes to use the shape parameters $\alpha = 0.697$ and $\beta = 3.27$ for short-period planets, which show a larger fraction of low-eccentricity

[5] https://github.com/nespinoza/ld-exosim/

orbits. I adopted these values and used Equation 4.9 as a prior for e. For comparison, I also performed a fit with a uniform prior. Figure 4.4 shows the marginalized posterior distributions of e for both runs, together with $P(e)$. Both distributions strongly favor a low eccentricity. This result is consistent with tidal circularization, which can take place on timescales shorter than the lifetime of the system by tidal interaction of close-in giant planets with their host star (Trilling 2000). As derived from Goldreich & Soter (1966), this timescale is given by

$$\tau_{\mathrm{circ}} = \frac{4}{63} Q_p \left(\frac{a^3}{G M_\star} \right)^{1/2} \left(\frac{M_p}{M_\star} \right) \left(\frac{a}{R_\mathrm{p}} \right)^5, \tag{4.10}$$

where a is the semi-major axis of the planet, G is the gravitational constant, $M_\star$ is the mass of the host star, M_p is the mass of the planet, and Q_p is the planet's tidal lag. The distribution of eccentricities of known short-period giant planets further strengthens the zero-eccentricity hypothesis. More than 80 % of the planets with $R_\mathrm{p} > 0.5\,R_\mathrm{Jup}$ and $P < 2.0\,\mathrm{d}$ in the NASA Exoplanet Archive (Akeson et al. 2013) have eccentricities lower than $e = 0.05$ (compare Figure A.3). Therefore, I assume a circular orbit of EPIC 217393088 and fixed ω to arbitrary 90° for all of the following analysis.

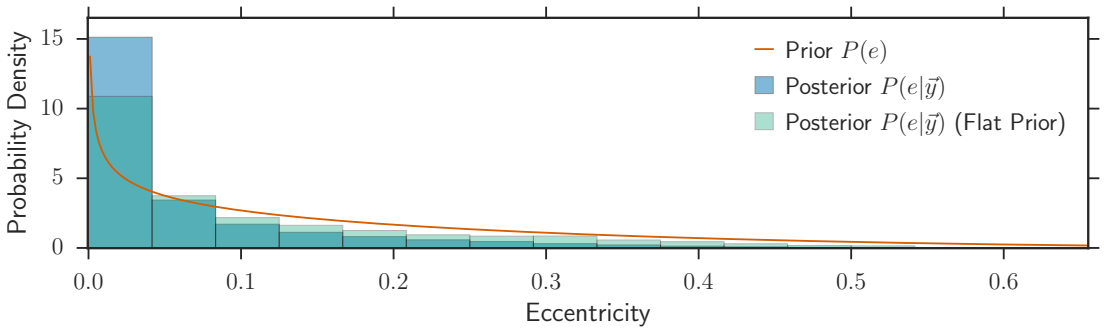

Figure 4.4.: Prior and posterior probability distribution for the orbital eccentricity. $P(e)$ is a Beta distribution with $\alpha = 0.697$ and $\beta = 3.27$ and served as a prior for the fit that resulted in the blue posterior distribution $P(e|\vec{y})$. The fit corresponding to the green histogram adopted a flat prior for e.

Prior Probabilities

For all remaining free parameters, I adopted priors that are uninformative but prohibited non-physical solutions by the choice of appropriate bounds. I enforced the following requirements via *log likelihood penalization* (Kipping & Sandford 2016), i.e. adding a logarithmic prior $\log P(\theta) = \log P(b) + \log P(R_\mathrm{p}/R_\star) + \log P(a/R_\star)$ to the logarithmic likelihood $\log \mathcal{L}(\theta)$.

The existence of a transit implies that the impact parameter must obey

$$|b| = |a/R_\star \cos i| < 1 + R_\mathrm{p}/R_\star, \tag{4.11}$$

giving rise to the log prior

$$\log P(b) = \begin{cases} 0, & \text{if} \quad |b| < 1 + R_\mathrm{p}/R_\star; \\ -\infty, & \text{otherwise.} \end{cases} \tag{4.12}$$

Similarly, the planet size should be positive and (by definition) not larger than the size of the star, i.e.

$$\log P(R_\mathrm{p}/R_\star) = \begin{cases} 0, & \text{if} \quad 0 \leq R_\mathrm{p}/R_\star \leq 1; \\ -\infty, & \text{otherwise.} \end{cases} \tag{4.13}$$

In addition, the planet should not be in contact with the star, thus I set

$$\log P(a/R_\star) = \begin{cases} 0, & \text{if} \quad a/R_\star > 1 + R_\mathrm{p}/R_\star; \\ -\infty, & \text{otherwise.} \end{cases} \tag{4.14}$$

For the remaining parameters u_0, u_1, and t_0, I adopted uniform priors.

MCMC Analysis

The likelihood function was chosen according to Equation 2.7, where I set the uncertainty σ to the standard deviation of the detrended out-of-transit flux. I used the MCMC sampler `emcee` (Foreman-Mackey et al. 2013) to sample the parameter space with 450 "walkers" (Goodman & Weare 2010), each of which exploring for 250 iterations after a burn-in phase of 100 steps. To mitigate correlation between the samples, I kept only every 10th iteration. The correlation length[6] of the thinned Markov chain ranged from 7 to 10, corresponding to an effective sample size of 1100 to 1600 per parameter.

In Figure 4.5, I visualize all one- and two-dimensional projections of the posterior in a corner plot[7]. It shows the marginalized distributions of all parameters used for the fit as well as the covariances between them. For all parameters, I give the 50th percentile of the respective marginalized posterior distribution as the result and quote their 16th and 84th percentiles as uncertainties. One can immediately see that the best constrained parameter is the time of inferior conjunction t_0. It does not show any significant correlations to other parameters. Its best-fit value of 0.4991 ± 0.0004 in phase units translates into a determination of the mid-transit time with 45 s precision. There is, however, a positive correlation between the planet-to-star ratio $R_\mathrm{p}/R_\star$ and the scaled semi-major axis $a/R_\star$. This is not surprising: The transit duration is, by simple geometric consideration, directly proportional to R_p and inversely proportional to the transverse component of the relative orbital velocity. The latter in turn is, from Kepler's second law, inversely proportional to the distance from the star to the planet at the time of conjunction. This

[6] computed using `acor` (Goodman & Weare 2010), https://github.com/dfm/acor
[7] created with `corner.py` (Foreman-Mackey 2016), http://corner.readthedocs.io

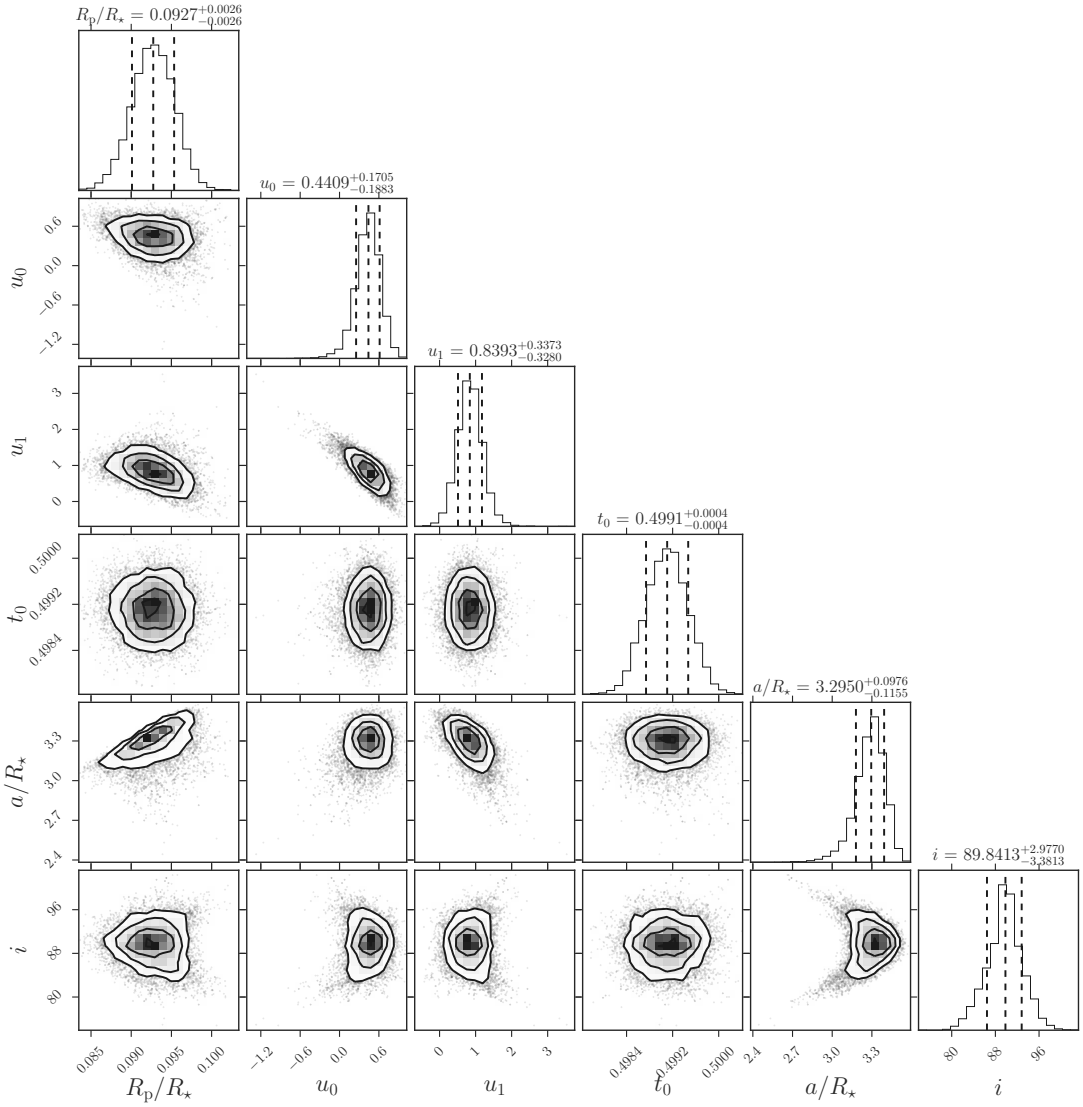

Figure 4.5.: Corner plot showing posterior probability distributions (along diagonal) and covariances (off-diagonal) of all parameters of interest in the EPIC 217393088 system.

degeneracy can not be lifted without complementary data, e.g. from precise RV measurements. In addition, $R_p/R_\star$ is correlated with the orbital inclination i, since any positive or negative deviation from an edge-on configuration ($i = 90°$) will result in a shorter transit duration. This explains the fairly symmetric shape of the correlation plots involving i. I infer from the largely normally distributed samples a planet-to-star ratio of $R_p/R_\star = 0.0927 \pm 0.0026$. The marginalized distribution of $a/R_\star$ is somewhat skewed from the strong correlation with i. By the same argument as above, both $a/R_\star$ and i are a function of transit duration. We are observing this planetary system nearly edge-on with $i = 89.8^{+3.0}_{-3.4}\,°$. Under the assumption of zero eccentricity, the scaled orbital radius

of the planet amounts to $a/R_\star = 3.30^{+0.10}_{-0.12}$. For the limb darkening parameters, I found $u_0 = 0.44^{+0.17}_{-0.19}$ and $u_1 = 0.84^{+0.34}_{-0.33}$. All transit parameters are listed in Table 4.2.

4.3.5. Host Star Analysis

I determined the effective temperature of the star using `TeffFit` and photometry listed on ExoFOP. The goodness of fits for giant ($\chi^2_{\mathrm{avg}} = 4.94$) and supergiant ($\chi^2_{\mathrm{avg}} = 3.07$) templates yielded less satisfactory solutions compared to $\chi^2_{\mathrm{avg}} = 1.58$ for luminosity class V. Under the assumption that the object is a dwarf star, its effective temperature is $(5449 \pm 42)\,\mathrm{K}$ (see Figure 4.6). This is more than 500 K lower than the value from the EPIC (Huber et al. 2016), $(5981 \pm 176)\,\mathrm{K}$. To investigate this discrepancy, I performed an SED fit to all available photometry using the VOSA tool and an ATLAS9 stellar model (Castelli & Kurucz 2004). The fit yielded a photospheric temperature of $(5500 \pm 150)\,\mathrm{K}$, consistent with our result. A black body fit to the photometry gave $T_{\mathrm{eff}} = (5550 \pm 100)\,\mathrm{K}$. Huber et al. infer their properties of EPIC 217393088 based on reduced proper motion and broadband colors. They report a possible overestimation of E_{B-V} in their analysis for near stars in Campaigns with a FOV close to the Galactic plane, which is the case for C7 (see Figure 2.3). Indeed, the extinction listed in the EPIC, $E_{B-V} = 0.1669\,\mathrm{mag}$, is much higher than the value in Schlafly & Finkbeiner (2011) at these coordinates, who report $E_{B-V} = (0.0861 \pm 0.0049)\,\mathrm{mag}$. Thus, I suspect that the target was de-reddened too much in the spectral typing procedure of Huber et al. (2016), giving rise to an SED that fits a hotter star. I adopt the temperature of `TeffFit`, which classifies EPIC 217393088 as a G8V star (Mamajek et al. 2012).

Although I can not reliably constrain other stellar parameters such as $M_\star$, $R_\star$, $\log g$, or the density ρ without additional information, I estimated the stellar radius using the empirical temperature-radius relation in Boyajian et al. (2012). I do not provide uncertainties for this estimate since the missing covariances in the relation impede a proper error propagation. I found $R_\star \approx 0.81\,R_\odot$, which translates into a planetary radius $R_{\mathrm{p}} = 0.73\,R_{\mathrm{Jup}}$, i.e. roughly the size of Saturn.

4.3.6. Equilibrium Temperature

The stellar radius estimate suggests a remarkably close orbit with $a = 0.012\,\mathrm{AU}$ for the planet; this is about 1/30 of the orbital radius of Mercury. Such proximity to the host star is naturally accompanied by immense irradiance, leading to high temperatures especially on the planet's day side. The temperature profile of this close-in exoplanet is a function of many unconstrained parameters, including the albedo, intrinsic luminosity, chemical composition, and the efficiency of heat redistribution across the planet (Sudarsky et al. 2002). While such detailed meteorology is beyond the context of this thesis, we can

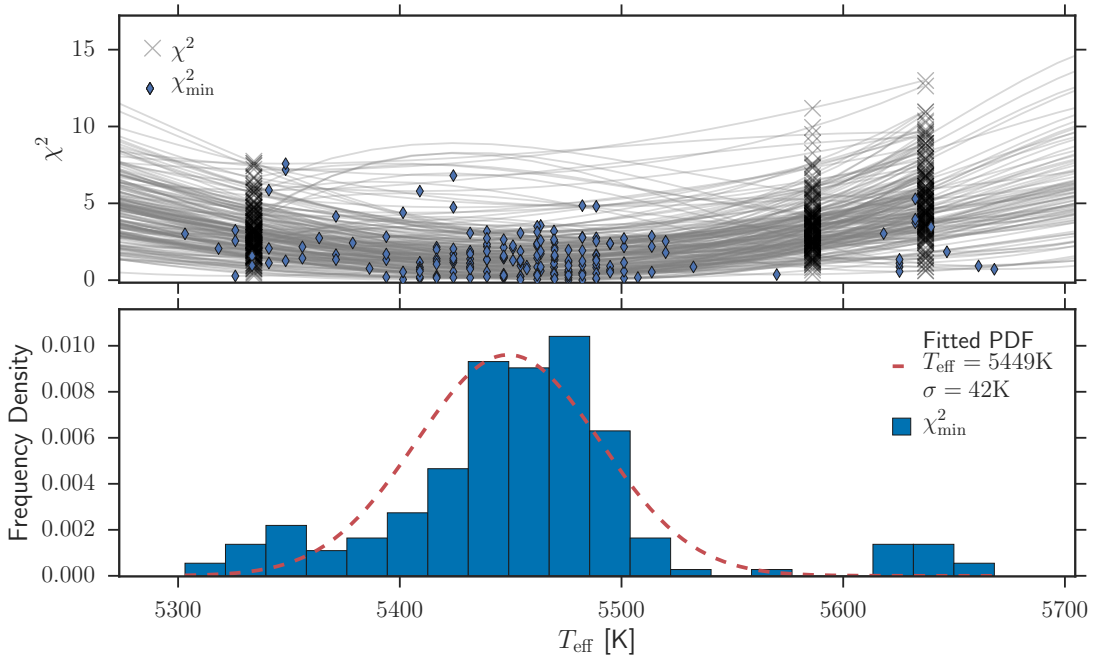

Figure 4.6.: Effective temperature fit of EPIC 217393088 with `TeffFit`. The magnitudes for this fit were queried from ExoFOP. *Top:* Goodness of fit results for template stars (gray crosses) and interpolated χ^2 (gray lines). Blue diamonds indicate the minima of the interpolations. *Bottom:* Histogram of χ^2 minima. A Gaussian PDF (red dashed line) is fit to the histogram to obtain a mean effective temperature of 5449 K with $\sigma = 42$ K.

estimate an equilibrium temperature $T_{\rm eq}$ that the planet would have if it was a zero-albedo black body with no intrinsic luminosity. This temperature is given by

$$T_{\rm eq} = \frac{\sqrt{R_\star}\, T_{\rm eff}}{\sqrt{2a}(1-e)^{1/8}} \tag{4.15}$$

if the planet re-radiates from its entire surface area (Fischer et al. 2015). The equilibrium temperature of EPIC 217393088.01 amounts to $T_{\rm eq} = 2120$ K.

4.3.7. Missing Secondary Eclipse

Despite the short orbit period that guarantees a strong irradiance, there are no visible signatures of phase variations (modulations of the light from the planet as it orbits the star) or secondary eclipses (occultations of the planet by the star). To see this periodic switch-off of the light from the planet, its amplitude has to be higher than the photometric noise in the light curve.

Radiation from a planet consists of its thermal emission and starlight reflected from the planet. The ratio of these fluxes is strongly wavelength-dependent: While the thermal

emission of a hot Jupiter peaks at several µm, their reflected light dominates in regimes of shorter wavelengths such as in the *Kepler* response band (Rouan et al. 2011). Neglecting the thermal contribution, the ratio of the flux reflected from the exoplanet $F_{\mathrm{p},\lambda}$ to the flux from the star $F_{\star,\lambda}$, i.e. the expected amplitude of the secondary eclipse signal, can be approximated by

$$\delta_{\mathrm{SE,\,reflected}} = \frac{F_{\mathrm{p},\lambda}}{F_{\star,\lambda}} \approx \left(\frac{R_{\mathrm{p}}}{a}\right)^2 p_\lambda, \tag{4.16}$$

where p_λ is the wavelength-dependent geometric albedo (Cowan et al. 2007). In the extreme case of $p_\lambda = 1$, and using the best-fit parameters from Section 4.3.3, Equation 4.16 yields $\delta_{\mathrm{SE,\,reflected}} \approx 7.9 \times 10^{-4} = 790\,\mathrm{ppm}$, comparable to the RMS deviation of the detrended light curve. However, this high-reflectance scenario is questionable since gas giants have shown to be dark in the visible (Sudarsky et al. 2002; Demory et al. 2011). The high temperature of this planet makes a detectable signal of the phase curve in the infrared likely.

4.3.8. Discussion

My analysis allows the conclusion that the signatures in the light curve of EPIC 217393088 are caused by a giant gas planet with an orbital period of $P = (1.3195 \pm 0.0048)\,\mathrm{d}$. If the estimated stellar radius of $R_\star = 0.81\,R_\odot$ is taken at face value, the inferred absolute orbital radius of $a = 0.012\,\mathrm{AU}$ makes EPIC 217393088.01 one of the closest-orbiting exoplanets ever detected and the only giant planet with such a small orbital radius[8]. The proximity to the host star leads to a hot and extreme environment at the position of the planet, which has an equilibrium temperature $T_{\mathrm{eq}} = 2120\,\mathrm{K}$.

The size of the orbit is of the same order as the size of the star; thus, the gravitational force of the star varies significantly across the volume of the planet. Such systems are expected to be subject to tidal locking of the planet's rotational period to the orbital period, i.e. one side of the planet always faces the star (Gladman et al. 1996). By the same tidal forces, energy is dissipated and angular momentum of the orbital movement is transferred to the stellar spin. This effect causes planets on orbits of very short periods to spiral in toward their host (Rodríguez & Ferraz-Mello 2010), in rare occasions even on detectable timescales (see e.g. Maciejewski et al. 2016). Computing an absolute timescale τ_a for this process is challenging due to the large uncertainty in $Q'_\star$, which is the ratio between the present annual tidal quality factor $Q_\star$ and the tidal Love number of degree 2, $k_{2,\star}$ (typically $10^5 < Q'_\star < 10^{10}$, Pätzold et al. 2004). However, τ_a is very sensitive to the semi-major axis with $\tau_a \sim a^5$ (Levrard et al. 2009). With better knowledge about the star, it could be evaluated if τ_a is small enough to detect the orbital decay on timescales of years or decades.

As discussed in Section 4.3.7, the chances are high to observe a phase curve and secondary eclipses in longer wavelengths than the *Kepler* band provides. If done in more than one

[8] as of December 12, 2016; NASA Exoplanet Archive (Akeson et al. 2013)

Parameter	Value[a]	Source
Literature		
K2 Campaign	7	A
Right Ascension (J2000)	+19 h 17 m 45.39 s	A
Declination (J2000)	−20 h 39 m 15.75 s	A
2MASS Designation	J19174538-2039156	A
Kepler magnitude Kp [mag]	15.293	A
Orbital Parameters		
Period P [d]	1.3195 ± 0.0048	B
Eccentricity[b] e	0.0	C,D
Inclination i [°]	$89.8^{+3.0}_{-3.4}$	D
Scaled Semi-Major Axis $a/R_\star$	$3.30^{+0.10}_{-0.12}$	D
Semi-Major Axis a [AU]	0.012	D,E
Planetary Parameters		
Scaled Planetary Radius $R_\mathrm{p}/R_\star$	0.0927 ± 0.0026	D
Planetary Radius R_p [R_Jup]	0.73	D,E
Equilibrium Temperature T_eq [K]	2120	E,F,G
Stellar Parameters		
Effective Temperature T_eff [K]	5449 ± 42	G
Linear Limb Darkening u_0	$0.44^{+0.17}_{-0.19}$	D
Quadratic Limb Darkening u_1	$0.84^{+0.34}_{-0.33}$	D
Radius $R_\star$ [$R_\odot$]	0.81	E

[a] Uncertainties correspond to 16 % and 84 % quantiles.
[b] The orbital eccentricity was held to zero, following the discussion in Section 4.3.4.
A: EPIC
B: Periodogram in Section 4.3.2
C: Following the discussion in Section 4.3.4
D: MCMC analysis in Section 4.3.4
E: Based on empirical estimate (see Section 4.3.5)
F: Assuming a circular orbit, zero albedo, no intrinsic luminosity, and perfect heat redistribution (see Section 4.3.6)
G: Photometric fit with `TeffFit`

Table 4.2.: System parameters for EPIC 217393088.

filter band, it is possible to construct an SED of the light emitted by the planet from these observations. Due to its tight orbit and hot surface temperature, EPIC 217393088.01 is also likely one of the few planets suitable for emission spectroscopy (Stevenson et al. 2014).

The extreme parameters of this planet can also cause dust emission and might ultimately lead to its disruption (e.g. Li et al. 2010; Sanchis-Ojeda et al. 2015). Although such events are relatively rare (Sanchis-Ojeda et al. 2015), the high irradiance of EPIC 217393088.01 makes it a potential candidate for detection of these effects.

4.4. EPIC 220262993: Irregular Dips

EPIC 220262993 was observed in K2 Campaign 8 in long cadence mode. It is located at RA = 01h 03m 30.92s, Dec = 01h 50m 41.7s (J2000 coordinates) and has a baseline magnitude of $m_{\mathrm{Kep}} = 18.78$. The target was flagged by `lcps`, since its K2SFF light curve shows isolated dips in flux of up to $\sim 25\,\%$ (see Figure 4.7).

4.4.1. K2 Light Curve and Contamination Check

The strongest features are two steep, V-shaped dips in the first third of the photometry that are not periodic within the 79 d observation. The first of these dips shows a dimming rate of $-72\,\%\,\mathrm{d}^{-1}$, whereas the rate of the second dip amounts to $-21\,\%\,\mathrm{d}^{-1}$.

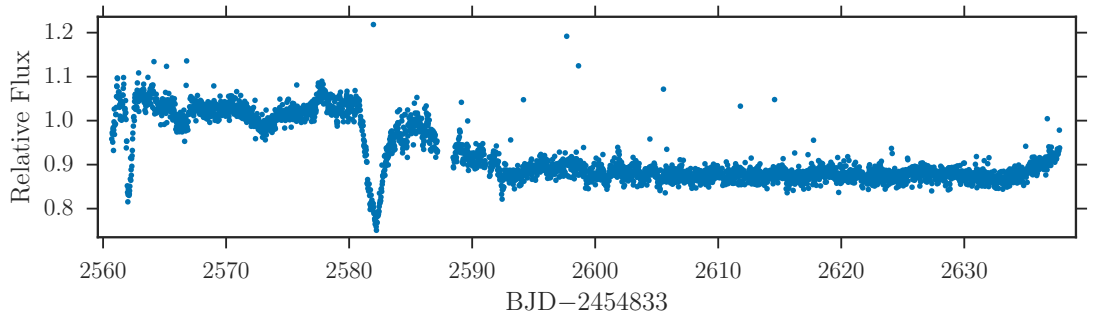

Figure 4.7.: K2SFF light curve of EPIC 220262993. Besides small-scale variabilities, the light curve exhibits two dramatic V-shaped dips of 0.8 d and 2.8 d duration, respectively. During the larger of these dimming events, a maximum of 25 % of the total flux disappears.

I checked the PDC data to make sure the signal does not stem from the K2SFF detrending process. It is present in these data as well with very similar shape. An inspection of the flux time series of the individual pixels in the target mask did not reveal any anomalies (see Figure B.1). I also obtained the EVEREST data of EPIC 220262993 for a cross-check. Their processed light curve preserves the two major dips, albeit shallower than in the PDC and K2SFF data. EVEREST's contamination statistics shows no signs of

light from background or foreground sources in the aperture (see Figure B.2). Available archival images show no bright nearby companions within the K2 aperture (compare Figure 4.8). The object is known, however, its classifications based on optical and mid-

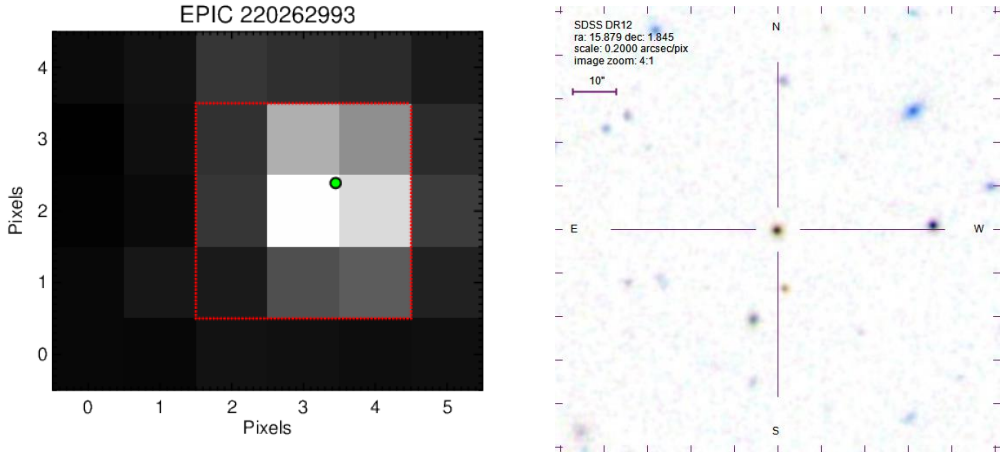

Figure 4.8.: Contamination analysis of EPIC 220262993. *Left panel:* Coadded image of all K2 cadences. The red region encloses the 'best' photometric aperture used for the K2SFF product; the green dot denotes the position of the object according to the astrometry information from the *Kepler* target pixel file. There are no conspicuous features visible in the point spread function (PSF). Credit: Andrew Vanderburg. *Right panel:* SDSS Finder Chart for EPIC 220262993. This image from SDSS, data release 10, shows the environment within 80″ of EPIC 220262993. There are no nearby companions visible.

infrared colors are inconsistent: It was identified as a possible quasi-stellar object (QSO; Crampton et al. 1997; Brescia et al. 2015; Richards et al. 2015) and as a white dwarf (WD; Gentile Fusillo et al. 2015). It is also listed in the initial Gaia source list with nearly zero proper motions, $(\mu_{\mathrm{RA}};\ \mu_{\mathrm{Dec}}) = (2.1 \pm 6.2;\ -5.6 \pm 6.2)\,\mathrm{mas\,yr^{-1}}$ (Smart & Nicastro 2014), which favors it being an extragalactic object. An analysis with `TeffFit` did not yield consistent results, and there was no spectroscopic data available. To reveal the nature of EPIC 220262993, we conducted a series of follow-up observations.

4.4.2. Photometry: GROND

We observed EPIC 220262993 in seven bands using GROND. This instrument allows simultaneous exposures in four optical channels $(g', r', i',\ z')$ and three near-infrared channels (J, H, K). It is mounted on the MPI/ESO 2.2 m telescope in La Silla, Chile. On October 19, 2016, we took a single exposure of the target in each band. Table 4.3 shows the magnitudes from this observation and, for comparison, listed magnitudes. The optical channels are from SDSS, near-infrared (NIR) channels stem from the UKIRT Infrared Deep Sky Survey (UKIDSS) catalog. Apart from the g' band, the object appeared ~ 0.1 mag brighter in all GROND measurements (note that UKIDSS magnitudes are

Band	SDSS/UKIDSS magnitude	GROND AB magnitude
g'	18.885 ± 0.009	18.69 ± 0.02
r'	18.740 ± 0.010	18.62 ± 0.01
i'	18.622 ± 0.011	18.56 ± 0.01
z'	18.608 ± 0.033	18.50 ± 0.01
J	$17.751^{\dagger}$	18.54 ± 0.03
H	$17.077^{\dagger}$	18.30 ± 0.07
K	$16.655^{\dagger}$	18.78 ± 0.12

† Vega photometric system

Table 4.3.: Multi-band photometry of EPIC 220262993. I list magnitudes from the SDSS and UKIDSS catalogs together with our observations with the GROND instrument. Our data are generally brighter than the previous observations (note that UKIDSS magnitudes are given in the Vega system).

given in the Vega photometric system). There is no significant color change between the listed values and our measurements.

The SED from these data is not blue enough for a typical WD. The larger amplitude in g' strengthens the QSO hypothesis. The observed flat SED in the NIR is not a common feature of these objects, as it would imply either a strong contribution of the host galaxy or substantial dust emission (Greiner 2016). We could not sufficiently distinguish between a QSO and a WD without additional observations.

4.4.3. Low-Res Spectroscopy: FIRE

In order to distinguish the possible cases for EPIC 220262993, we obtained a NIR spectrum of this object. It was observed with the Folded-port InfraRed Echellette (FIRE) spectrometer mounted on the Magellan Baade 6.5 m telescope at the Las Campanas Observatory in Chile in the night of October 26, 2016. FIRE was set to High-Throughput Prism Mode, which resulted in a spectrum with spectral resolving power $R = 300 - 500$ spanning 0.8 µm to 2.5 µm wavelengths with a $1''$ slit width (Simcoe et al. 2013). Five 120 s exposures were obtained in ABBA nodding sequence and reduced with the facility pipeline. The reduction included flat fielding, sky subtraction, extraction of one-dimensional spectra, their wavelength calibration with NeAr lamp spectra, and a telluric correction. For the latter we used the A-type star BD-18 220, observed just before the science target. The final spectrum is shown in Figure 4.9. It shows a feature at ~ 1.5 µm that, upon inspection, appears only in the spectra from the nodding side B and is most likely a detector artifact. Apart from this feature, the spectrum is flat. The SNR at the continuum level is too low to draw conclusions as to whether EPIC 220262993 is a white dwarf, a QSO, or something else.

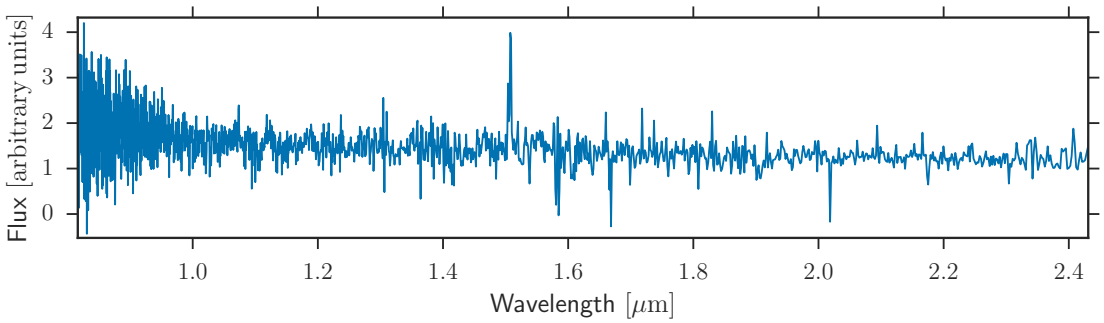

Figure 4.9.: NIR spectrum of EPIC 220262993, taken with the FIRE spectrometer on the Magellan Baade telescope. The spectrum is flat, except of a feature at $\sim 1.5\,\mu$m that we relate to a detector artifact.

4.4.4. Echellette Spectroscopy: ESI

On November 19, 2016, we observed EPIC 220262993 in the optical with the Echellette Spectrograph and Imager (ESI, Sheinis et al. 2002) at the Keck II 10 m telescope on the Mauna Kea summit, Hawaii. A slit width of $1''$ was chosen, corresponding to a resolution of ~ 4000. The target was observed with a single exposure of 900 s duration. We used the MAKEE[9] package to reduce the data and calibrated the spectrum with the flux calibration star BD+284211. A wavelength binning of $5 \times 10^{-4}\,\mu$m was applied, and overlapping Echelle orders were averaged using a median filter to create the combined spectrum (Figure 4.10) with a usable coverage from 0.4 µm to 1.0 µm. We shifted the

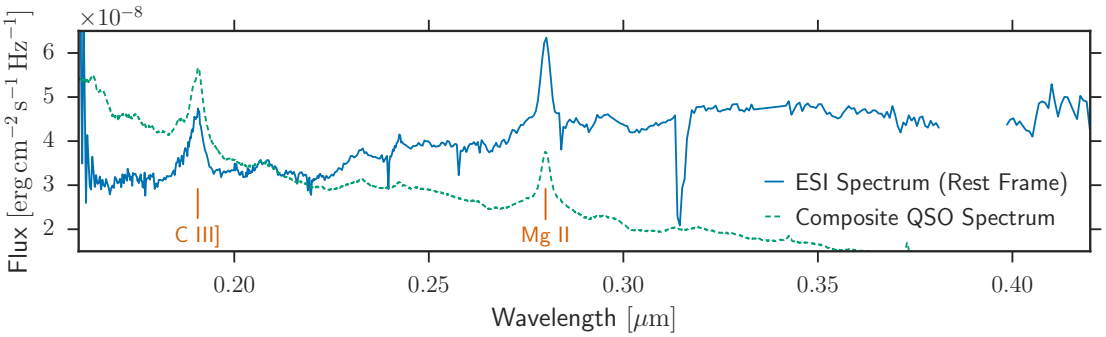

Figure 4.10.: Optical spectrum of EPIC 220262993, taken with the ESI spectrograph on the Keck II telescope. The measured spectrum (blue line) was shifted into the rest frame of a synthetic QSO spectrum at $z = 1.42$ (dashed green line). Two prominent features in the ESI spectrum correspond to the C III] and Mg II emission lines, respectively. The ESI spectrum is flatter compared to the composite spectrum, suggesting a substantial continuum contribution of the host galaxy.

[9] MAuna Kea Echelle Extraction, http://www.astro.caltech.edu/~tb/ipac_staff/tab/makee/index.html

spectrum in wavelength into the rest frame of a composite QSO spectrum (Vanden Berk et al. 2001) at $z = 1.42$. Two prominent features in the ESI spectrum correspond to broad emission lines at 0.19 µm (C III]) and at 0.28 µm (Mg II) in this composite. The agreement of these features allows us to draw the conclusion that the object is a quasar. Our observed spectrum is flatter, presumably due to a strong continuum contribution of the host galaxy.

4.4.5. Discussion

The brightnesses of a large number of quasars have been monitored from the ground (e.g. with OGLE, Sumi et al. 2005; MACHO, Kim et al. 2011; and other surveys), but they typically lack either the SNR or the cadence to detect flux variations comparable to the features in EPIC 220262993's light curve. Only few quasars have been observed with an accuracy and cadence comparable to *Kepler*'s (e.g. Mushotzky et al. 2011), and none of them exhibit variations with 20 % to 25 % amplitude on timescales of hours. There have been claims of intraday variability for a few powerful radio loud quasars (e.g. Foschini et al. 2015). EPIC 220262993, however, was not detected in the FIRST survey, which was carried out at 1400 MHz (Becker et al. 1994). Adopting a ΛCDM cosmology with $H_0 = 70$ and $\Omega_M = 0.286$, its detection limit for $z = 1.42$ translates to a spectral luminosity $L_6 \lesssim 10^{24.5}\,\mathrm{W\,Hz^{-1}}$. The criterion for radio loud quasars is $L_6 \gtrsim 10^{23.2}\,\mathrm{W\,Hz^{-1}}$ (Kellermann et al. 2016), suggesting that this object is either a radio quiet QSO or a weak radio loud QSO. Even among radio loud quasars, a drop in flux of this magnitude has not been seen (Capellupo et al. 2013).

The cause of the irregular dimming events remains unclear. Their short timescales make a physical process taking place inside the quasar's continuum emitting region unlikely, since the dimensions of this region are in the ballpark of 0.02 pc (Wayth et al. 2008), which translates into about three light weeks. Thus, any synchronized emission process across the entire volume can not happen on timescales faster than three weeks since the synchronization is limited by the light travel time. Variations of shorter timescales can occur in radio loud quasars, which exhibit emission from more compact regions and collimated jets. Another possible explanation is an occultation event by one or several opaque bodies or a dust cloud in the vicinity of the QSO. In this case, the transiting object must cover more than 20 % of the emitting region to account for the depth of the dips.

5. Conclusions and Outlook

In this chapter, I summarize what I have accomplished and conclude by looking at possible future extensions of this work.

I developed an algorithm that determines the effective temperature of an object from available multi-band photometry. A number of tests showed that it successfully recovers the temperature of synthetic stars and agrees with results of other methods. Ongoing work builds on this capability and extends `TeffFit` towards an estimate of distance and extinction from photometry alone. First tests show a reasonable distribution of distances and extinctions among the involved luminosity classes. The long-term goal is to obtain a more accurate Galactic dust reddening along a specific line of sight than possible with currently available grids.

I used this software to characterize the host star of a planetary candidate I discovered, which allowed me to estimate physical parameters of this extrasolar system. The results of my analysis are consistent with a Saturn-sized planet in a circular orbit with a radius of only 0.012 AU, making EPIC 217393088.01 the giant planet with the tightest orbit discovered to date. However, additional observations are needed to rule out possible astrophysical false positives and confirm the planetary origin of the transit signal. The next step will be to obtain additional transit photometry in multiple filter bands. As opposed to an eclipsing binary system, planetary transits produce the same depth in all wavelengths since they only block stellar light and do not contribute significant own radiation. We also plan to conduct low-resolution spectroscopic observations in order to get an estimate of the RV amplitude. To ultimately confirm the discovery, we need to detect an RV signal by employing high-resolution spectroscopy. This would also yield constraints on the stellar and planetary masses and improve the accuracy of the parameters derived in this work. While I found no evidence of TTVs within the ~ 79 d baseline of K2 long cadence data, the extremely tight orbit of EPIC 217393088.01 potentially offers the opportunity of observing the decay of its orbit and possibly a progressive tidal disruption by the host star.

Furthermore, I created a tool to find dips in time series regardless of their shape. My software `lcps` is compatible with any time series data; it has been successfully applied to K2 long cadence photometry. To quantitatively assess the detection performance, I plan to test the algorithm by injecting transit signatures with a broad range of shapes and amplitudes.

The `lcps` software led to an enigmatic finding: I discovered an unidentified object that exhibits steep dips in flux of up to 25 % with no apparent periodicity. Follow-up observations using multi-band photometry, as well as optical and NIR spectroscopy revealed the extragalactic nature of EPIC 220262993 and allowed us to classify it as a quasar at $z = 1.42$ that is either radio quiet or only weakly emitting in radio bands with $L_6 \lesssim 10^{24.5}\,\mathrm{W\,Hz^{-1}}$. It is the first such object with deep dips in flux on hour timescales. Further photometric monitoring is crucial to detect future dimming events and learn if they occur periodically or not. If they do, it should be assessed whether the dips change their shape and/or depth in order to gain knowledge about the physical processes that cause them. Continuous long-term monitoring will become available at the latest through the Large Synoptic Survey Telescope (LSST), which will enable a revisit time of 3 d to 4 d (Ivezic et al. 2008). In case EPIC 220262993 is the progenitor of a new class of objects, there is a high chance that more of them will by detected in future.

Bibliography

A. F. M. Smith, D. J. S. 1980, Journal of the Royal Statistical Society. Series B (Methodological), 42, 213

Akeson, R. L., Chen, X., Ciardi, D., et al. 2013, Publ. Astron. Soc. Pacific, 125, 989

Alonso, A., Arribas, S., & Martínez-Roger, C. 1999, Astron. Astrophys. Suppl. Ser., 140, 261

Alonso, R., Auvergne, M., Baglin, A., et al. 2008, Astron. Astrophys., 482, 21

Anglada-Escudé, G., Amado, P. J., Barnes, J., et al. 2016, 437–440, doi:10.1038/nature19106

Ansdell, M., Gaidos, E., Rappaport, S. A., et al. 2016, Astrophys. J., 816, 69

Bailer-Jones, C. A. L. 2011, Mon. Not. R. Astron. Soc., 411, 435

Basri, G., Walkowicz, L. M., Batalha, N., et al. 2011, AJ, 141, 20

Batygin, K., & Brown, M. E. 2016, Astron. J., 151, 22

Becker, R. H., White, R. L., & Helfand, D. J. 1994, in Astronomical Society of the Pacific Conference Series, Vol. 61, Astronomical Data Analysis Software and Systems III, ed. D. R. Crabtree, R. J. Hanisch, & J. Barnes, 165

Bedding, T. R., Mosser, B., Huber, D., et al. 2011, Nature, 471, 608

Bochanski, J. J., & Claire, M. W. 2010, in Bulletin of the American Astronomical Society, Vol. 42, American Astronomical Society Meeting Abstracts #215, 288

Bodman, E. H. L., & Quillen, A. 2016, Astrophys. J., 819, L34

Boffin, H. M. J. 2012, in Orbital Couples: Pas de Deux in the Solar System and the Milky Way, ed. F. Arenou & D. Hestroffer, 41–44

Borucki, W. J., Koch, D., Basri, G., et al. 2005, Science (80-.)., 327, 977

Boyajian, T. S., von Braun, K., van Belle, G., et al. 2012, Astrophys. J., 757, 112

Boyajian, T. S., LaCourse, D. M., Rappaport, S. A., et al. 2016, Mon. Not. R. Astron. Soc., 457, 3988

Brescia, M., Cavuoti, S., & Longo, G. 2015, Mon. Not. R. Astron. Soc., 450, 3893

Bruno, G. 1584, De l'infinito universo et mondi

Capellupo, D. M., Hamann, F., Shields, J. C., Halpern, J. P., & Barlow, T. A. 2013, Mon. Not. R. Astron. Soc., 429, 1872

Carpenter, J. M. 2001, Astron. J., 121, 2851

Carter, J. A., & Winn, J. N. 2009, Astrophys. J., 704, 51

Castelli, F., & Kurucz, R. L. 2004, ArXiv Astrophys. e-prints, xxx, 1

Charbonneau, D., Brown, T. M., Latham, D. W., & Mayor, M. 2000, Astrophys. J., 529, L45

Christiansen, J. L. 2013, 1
Claret, A. 2000, Astron. Astrophys., 363
Claret, A., & Hauschildt, P. H. 2003, Astron. Astrophys., 412, 241
Cody, A. M., & Sasselov, D. D. 2002, Astrophys. J., 569, 451
Covey, K. R., Ivezic, Z., Schlegel, D. J., et al. 2007, Astron. J., 134, 23
Cowan, N. B., Agol, E., & Charbonneau, D. 2007, Mon. Not. R. Astron. Soc., 379, 641
Crampton, D., Gussie, G., Cowley, A. P., & Schmidtke, P. C. 1997, Astron. J., 114, 2353
Cubillos, P., Harrington, J., Loredo, T. J., et al. 2016, arXiv:1610.01336
Demory, B.-O., Seager, S., Madhusudhan, N., et al. 2011, Astrophys. J. Lett., 715, 6
Diaz-Cordoves, J., & Gimenez, A. 1992, Astron. Astrophys., 259
Doi, M., Tanaka, M., Fukugita, M., et al. 2010, Aj, 139, 1628
Dressing, C. D., & Charbonneau, D. 2013, Astrophys. J., 767, 95+
Espinoza, N., & Jordán, A. 2016, Limb-darkening and exoplanets II: Choosing the Best Law for Optimal Retrieval of Transit Parameters
Evans, T. M., Sing, D. K., Wakeford, H. R., et al. 2016, Detection of H2O and evidence for TiO/VO in an ultra hot exoplanet atmosphere
Feigelson, E. D., & Babu, G. J. 2012, Modern Statistical Methods for Astronomy: With R Applications (Cambridge: Cambridge University Press), doi:10.1017/CBO9781139015653
Fischer, D. A., Howard, A. W., Laughlin, G. P., et al. 2015, Protostars Planets VI, 715
Fischer, D. A., Schwamb, M. E., Schawinski, K., et al. 2012, Mon. Not. R. Astron. Soc., 419, 2900
Fischer, P. D., Knutson, H. A., Sing, D. K., et al. 2016, arXiv:1601.04761
Foreman-Mackey, D. 2016, The Journal of Open Source Software, 24, doi:10.21105/joss.00024
Foreman-Mackey, D., Hogg, D. W., Lang, D., & Goodman, J. 2013, Publ. Astron. Soc. Pacific, 125, 306
Foschini, L., Berton, M., Caccianiga, A., et al. 2015, Astron. Astrophys., 575, A13
G. A. Barnard, G. M. Jenkins, C. B. W. 1962, Journal of the Royal Statistical Society. Series A (General), 125, 321
Gauss, C. F. 1816, Zeitschrift für Astron. und verwandte Wissenschaften, 1, 187
Gentile Fusillo, N. P., Gansicke, B. T., & Greiss, S. 2015, Mon. Not. R. Astron. Soc., 448, 2260
Gladman, B., Quinn, D. D., Nicholson, P., & Rand, R. 1996, Icarus, 122, 166
Goldreich, P., & Soter, S. 1966, Icarus, 5, 375
Goodman, J., & Weare, J. 2010, Commun. Appl. Math. Comput. Sci., 5
Greiner, J. 2016, private communication
Greiner, J., Bornemann, W., Clemens, C., et al. 2008, Publ. Astron. Soc. Pacific, 120, 405
Hartman, J. D., & Bakos, G. Á. 2016, arXiv:1605.06811
Haswell, C. 2010, Transiting Exoplanets (Cambridge University Press)

Herbst, W., & Shevchenko, V. S. 1999, Astron. J., 118, 1043
Howard, A. W., Marcy, G. W., Bryson, S. T., et al. 2012, Astrophys. J. Suppl. Ser., 201, 15
Howell, S. S. B., Sobeck, C., Haas, M., et al. 2014, ArXiv(1402.5163), 25
Hubbard, W. B., Fortney, J. J., Lunine, J. I., et al. 2001, Astrophys. J., 560, 413
Huber, D., Bryson, S. T., Haas, M. R., et al. 2016, Astrophys. J. Suppl. Ser., 224, 2
Ivanov, V. D., Rieke, M. J., Engelbracht, C. W., et al. 2004, Astrophys. J. Suppl. Ser., 151, 387
Ivezic, Z., Tyson, J. a., Acosta, E., et al. 2008, eprint arXiv, 0805, 2366
Jenkins, J. M., Caldwell, D. A., Chandrasekaran, H., et al. 2010, Astrophys. J., 713, L87
Jones, E., Oliphant, T., Peterson, P., et al. 2001–, SciPy: Open source scientific tools for Python, [Online; accessed 2016-10-22]
Kass, R. E., & Wasserman, L. 1996, J. Am. Stat. Assoc., 91, 1343
Kellermann, K. I., Condon, J. J., Kimball, A. E., Perley, R. A., & Ivezić, Ž. 2016, Astrophys. J., 831, 168
Kim, D.-W., Protopapas, P., Byun, Y.-I., et al. 2011, Astrophys. J., 735, 68
Kinemuchi, K., Fanelli, M., Pepper, J., Still, M., & Howell, S. B. 2012, Publ. Astron. Soc. Pacific, 124, 963
Kipping, D. M. 2011, PhD thesis, arXiv:1105.3189
—. 2013a, Mon. Not. R. Astron. Soc., 435, 2152
—. 2013b, Mon. Not. R. Astron. Soc. Lett., 434, 51
Kipping, D. M., & Sandford, E. 2016, Bayesian priors for transiting planets
Klinglesmith, D. A., & Sobieski, S. 1970, Astron. J., 75, 175
Koch, D. G., Borucki, W. J., Basri, G., et al. 2010, Astrophys. J., 713, L79
Kopal, Z. 1950, Harvard Coll. Obs. Circ., 454
Kovács, G., Zucker, S., Mazeh, T., et al. 2002, Astron. Astrophys., 391, 369
Kreidberg, L. 2015, 127, 1
Kroese, P. 2011, Handbook of Monte Carlo Methods
LaCourse, D. M., Jek, K. J., Jacobs, T. L., et al. 2015, Mon. Not. R. Astron. Soc., 452, 3561
Levesque, E. M., Massey, P., Olsen, K. A. G., et al. 2005, Astrophys. J., 628, 973
Levrard, B., Winisdoerffer, C., & Chabrier, G. 2009, Astrophys. J., 692, L9
Li, S.-L., Miller, N., Lin, D. N. C., & Fortney, J. J. 2010, Nature, 463, 1054
Lintott, C. J., Schwamb, M. E., Barclay, T., et al. 2013, Astron. J., 145, 151
Lisse, C. M., Sitko, M. L., & Marengo, M. 2015, Astrophys. J., 815, L27
Lomb, N. R. 1976, Astrophys. Space Sci., 39, 447
Luger, R., Agol, E., Kruse, E., et al. 2016, Astron. J., arXiv:1607.00524
Maceachern, S. N., & Berliner, L. M. 1994, The American Statistician, 48, 188
Maciejewski, G., Dimitrov, D., Fernández, M., et al. 2016, Astron. Astrophys., 588, L6
MacKay, D. J. C. 2005, Information Theory, Inference, and Learning Algorithms David J.C. MacKay, Vol. 100, 1–640, doi:10.1198/jasa.2005.s54

Mamajek, E., Quillen, A., Pecaut, M., et al. 2012, Astron. J., 143, 72
Mandel, K., & Agol, E. 2002, Astrophys. J., 580, L171
Mann, A. W., Gaidos, E., Kraus, A., & Hilton, E. J. 2013, Astrophys. J., 770, 43+
Masuda, K., & Suto, Y. 2016, Transiting planets as a precision clock to constrain the time variation of the gravitational constant
Mayor, M., & Queloz, D. 1995, Nature, 378, 355
McGinnis, P. T., Alencar, S. H. P., Guimarães, M. M., et al. 2015, arxiv Prepr. arXiv 1502.07692v2, 11, 27
Metropolis, N., Rosenbluth, A. W., Rosenbluth, M. N., Teller, A. H., & Teller, E. 1953, J. Chem. Phys., 21, 1087
Metropolis, N., & Ulam, S. 1949, The Monte Carlo Method, arXiv:44:335–341
Monet, D. 1996, in BAAS, Vol. 28, Bulletin of the American Astronomical Society, 1282
Montet, B. T., & Simon, J. D. 2016, arXiv:1608.01316
Mushotzky, R. F., Edelson, R., Baumgartner, W., & Gandhi, P. 2011, ApJ, 743, L12
Newton, I. 1687, Philosophiae Naturalis Principia Mathematica. Auctore Js. Newton, doi:10.3931/e-rara-440
Pätzold, M., Carone, L., & Rauer, H. 2004, Astron. Astrophys. (ISSN 0004-6361), 427, 1075
Pecaut, M. J., & Mamajek, E. E. 2013, Astrophys. J. Suppl. Ser., 208, 9
Perrin, G., Coudé du Foresto, V., Ridgway, S. T., et al. 1998, Astron. Astrophys., 626, 619
Petigura, E. A. 2015, PhD thesis, University of California, Berkeley
Pickles, A. J. 1998, Publ. Astron. Soc. Pacific, 110, 863
Pigulski, A., Pojmański, G., Pilecki, B., & Szczygieł, D. M. 2009, Acta Astron., 59, 33
Quintana, E. V., Jenkins, J. M., Clarke, B. D., et al. 2010, Proc. SPIE, 7740, 77401X
Rauer, H., Aerts, C., Cabrera, J., & PLATO Team. 2016, Astronomische Nachrichten, 337, 961
Richards, G. T., Myers, A. D., Peters, C. M., et al. 2015, Astrophys. J. Suppl. Ser., 219, 39
Ricker, G. R., Winn, J. N., Vanderspek, R., et al. 2014, arXiv, 9143, 914320
Rodríguez, A., & Ferraz-Mello, S. 2010, EAS Publ. Ser., 42, 411
Rouan, D., Deeg, H. J., Demangeon, O., et al. 2011, Astrophys. J. Lett., 17
Sackett, P. D. 1999, Planets Outs. Sol. Syst. Theory Obs. Ed. by J.-M. Mariotti D. Alloin. Dordr. ; Bost. Kluwer Acad. Publ., 189
Sanchis-Ojeda, R., Rappaport, S., Pallé, E., et al. 2015, eprint arXiv:1504.04379, 2
Savitzky, A., & Golay, M. J. E. 1964, Analytical Chemistry, 36, 1627
Scaringi, S., Manara, C. F., Barenfeld, S. A., et al. 2016, 9, 1
Schaefer, B. E. 2016, KIC 8462852 Faded at an Average Rate of 0.165+-0.013 Magnitudes Per Century From 1890 To 1989
Schlafly, E. F., & Finkbeiner, D. P. 2011, Astrophys. J., 737, 103
Schmitt, J. R., Agol, E., Deck, K. M., et al. 2014, Astrophys. J., 795, 167

Schwarzschild, K., & Villiger, W. 1906, Astrophys. J., 23, 284
Seager, S., & Sasselov, D. D. 2000, Astrophys. J., 537, 916
Seager, S., Turner, E., Schafer, J., & Ford, E. 2005, Astrobiology, 5, 372
Sedaghati, E., Boffin, H. M. J., Jeřabková, T., et al. 2016, 2, 1
Sheinis, A. I., Bolte, M., Epps, H. W., et al. 2002, Publ. Astron. Soc. Pacific, 114, 851
Simcoe, R. A., Burgasser, A. J., Schechter, P. L., et al. 2013, Publ. Astron. Soc. Pacific, 125, 270
Sing, D. K., Pont, F., Aigrain, S., et al. 2011, Mon. Not. R. Astron. Soc., 416, 1443
Skrutskie, M., Cutri, R., Stiening, R., et al. 2006, Astron. J., 131, 1163
Slipher, V. M. 1930, J. R. Astron. Soc. Canada, 24
Smart, R. L., & Nicastro, L. 2014, Astron. Astrophys., 570, A87
Stevenson, K. B., Désert, J.-M., Line, M. R., et al. 2014, Science (80-.)., 346
Struve, O. 1952, Obs., 72, 199
Sudarsky, D., Burrows, A., & Hubeny, I. 2002, Astrophys. J., 588, 1121
Sumi, T., Wo, P. R., Eyer, L., et al. 2005, 335, 331
Taylor, M. M. 2005, in Astronomical Society of the Pacific Conference Series, Vol. 347, Astron. Data Anal. Softw. Syst. XIV, ed. P. Shopbell, M. Britton, & R. Ebert, 29
Thompson, S. E. 2016
Thompson, S. E., Everett, M., Mullally, F., et al. 2012, ApJ, 753, 86
Trilling, D. E. 2000, Astrophys. J., 537, L61
Vacca, W. D., Garmany, C. D., & Shull, J. M. 1996, Astrophys. J., 460, 914
Vanden Berk, D. E., Richards, G. T., Bauer, A., et al. 2001, Astron. J., 122, 549
Vanderburg, A., & Johnson, J. A. 2014, Publ. Astron. Soc. Pacific, 126, 948
Vanderburg, A., Johnson, J. A., Rappaport, S., et al. 2015a, Nature, 526, 546
Vanderburg, A., Latham, D. W., Buchhave, L. A., et al. 2015b, 23
Wayth, B., Dowd, M. O., & Webster, R. L. 2008, 7, 1
Wien, W. 1896, Ueber die Energievertheilung im Emissionsspectrum eines schwarzen Körpers, doi:10.1002/andp.18962940803
Winn, J. N. 2010, eprint arXiv, 1001, 2010
Xu, S., Jura, M., Dufour, P., & Zuckerman, B. 2016, ApJ, 816, L22

List of Abbreviations

2MASS	Two Micron All Sky Survey. 22, 33, 35, 36
ASCII	American Standard Code for Information Interchange. 19
BJD	Barycentric Julian Day. 20, 35
BKJD	*Kepler* Barycentric Julian Day. 17, 19
BLS	Box Least Squares. 38, 41
CCD	Charge-Coupled Device. 12, 13, 17
EB	Eclipsing Binary. 18, 35
EPIC	Ecliptic Plane Input Catalog. 14, 19, 27, 28, 35, 41, 45
ESI	Echellette Spectrograph and Imager. 52, 53
EVEREST	EPIC Variability Extraction and Removal for Exoplanet Science Targets. 17, 49, 69
ExoFOP	Exoplanet Follow-up Observing Program. 28, 45, 46
FIRE	Folded-port InfraRed Echellette. 51
FITS	Flexible Image Transport System. 19
FOV	Field Of View. 12, 13, 45
FWHM	Full Width at Half Maximum. 12
GROND	Gamma-Ray Burst Optical/Near-Infrared Detector. 27, 29, 30, 50
HLSP	High Level Science Product. 16, 17
HWHM	Half width at half maximum. 38
JWST	James Webb Space Telescope. 8
K2SFF	K2 "Self-Flat-Fielding" corrected light curve. 15, 17, 19–21, 34–37, 49, 50
KOI	Kepler Object of Interest. 36
LSST	Large Synoptic Survey Telescope. 56
MAD	Median Absolute Deviation. 20
MAST	Mikulski Archive for Space Telescopes. 15–17, 71
MCMC	Markov Chain Monte Carlo. 11, 41, 43

MK	Morgan-Keenan spectral type. 22
MSE	Mean-squared error. 40
NIR	Near-Infrared. 50, 51, 56
PDC	Pre-Search Data Conditioning. 17, 19, 34–36, 39, 49, 70
PDF	Probability density function. 9, 25
ppm	parts per million. 6, 14
PSF	Point Spread Function. 50, 71
PyPI	Python Package Index. 19, 21
QSO	Quasi-stellar object. 50, 51, 53
RMS	Root mean square. 17, 37, 47
RV	Radial Velocity. 1, 2, 6, 44, 55
SDSS	Sloan Digital Sky Survey. 22, 50
SED	Spectral energy distribution. 27, 28, 45, 49, 51
SNR	Signal-to-noise ratio. 10, 12, 51, 53
TDV	Transit Duration Variation. 8
TTV	Transit Timing Variation. 8, 39, 55
UKIDSS	UKIRT Infrared Deep Sky Survey. 50
VOSA	VO SED Analyzer. 28, 45
WD	White dwarf. 50, 51
YSO	Young Stellar Object. 18

Acknowledgements

This research has made use of the VizieR and Simbad Astronomical Databases, operated at CDS, Strasbourg, France, and the Astrophysics Data System of NASA. It has made use of data products from the 2MASS Survey, which is a joint project of the University of Massachusetts and the Infrared Processing and Analysis Center/California Institute of Technology, funded by the National Aeronautics and Space Administration and the National Science Foundation. Further, I used services at the NASA Exoplanet Archive, which is operated by the California Institute of Technology, under contract with the National Aeronautics and Space Administration under the Exoplanet Exploration Program. This research has made use of the NASA/IPAC Infrared Science Archive, which is operated by the Jet Propulsion Laboratory, California Institute of Technology, under contract with the National Aeronautics and Space Administration. My thesis includes data collected by the K2 mission. Funding for the K2 mission is provided by the NASA Science Mission directorate. Some of the data presented in this work were obtained from the Mikulski Archive for Space Telescopes (MAST). STScI is operated by the Association of Universities for Research in Astronomy, Inc., under NASA contract NAS5-26555. Support for MAST for non-HST data is provided by the NASA Office of Space Science via grant NNX09AF08G and by other grants and contracts. This work makes also use of VOSA, developed under the Spanish Virtual Observatory project supported from the Spanish MICINN through grant AyA2011-24052, and PyKE (Still and Barclay 2012), a software package for the reduction and analysis of Kepler data. This open source software project is developed and distributed by the NASA Kepler Guest Observer Office. The MCMC run in Section 4.3.3 was performed using `emcee` (Foreman-Mackey et al. 2013), and the corner plot was made with `corner.py` (Foreman-Mackey 2016). Some of the data presented herein were obtained at the W.M. Keck Observatory, which is operated as a scientific partnership among the California Institute of Technology, the University of California and the National Aeronautics and Space Administration. The Observatory was made possible by the generous financial support of the W.M. Keck Foundation. I wish to recognize and acknowledge the very significant cultural role and reverence that the summit of Mauna Kea has always had within the indigenous Hawaiian community. We are most fortunate to have the opportunity to conduct observations from this mountain.

In the course of the last year, I enjoyed help and support by a lot of amazing people. They all contributed to this work in various ways and now, as I finish the last brush strokes, I want to thank them.

First and foremost, I owe a huge debt of gratitude to Prof. Jochen Greiner, who allowed me to take on this journey under his supervision. I am privileged to be supervised by a renowned researcher who left me the freedom to pursue my own ideas, but gently corrected my course when needed. I further appreciate his kind offer to observe with GROND on short notice. A big thank you goes to my supervisor at ESO, Valentin Ivanov, for tailoring a project that matched my interests and ambitions. He has been a inexhaustible source of guidance, always willing to share his knowledge about both the big picture and the technical details.

The PhD students at ESO established a refreshing work atmosphere. It was great fun to organize the Journal Club with some of you guys. In particular, I want to thank Na'ama for fruitful discussions about the periodogram, MCMC sampling, and transit models and for her immeasurable helpfulness. I offer a special thanks to Siyi for her efforts on observing our enigmatic dipper star, and for helping me with reducing and interpreting the spectra. I must not forget to thank the ESO staff, from IT to cleaning personnel, who ensured my stay here was pleasant and inspiring. I further acknowledge Alyssa for great linguistic advice that hugely improved the quality of this manuscript.

Ich möchte Dietrich Baade meinen besonderen Dank aussprechen. Du warst im vergangenen Jahr eine unerschöpfliche Quelle an Rat und bist mir ein echter Mentor geworden.

Ein großes Dankeschön geht an die Masterstudenten-Crew Julia, Robert, Moritz, Philipp und Sebastiano. Einige von euch haben durch das Lesen unzähliger Seiten viel zur Qualität dieser Arbeit beigetragen. Robert, ich bin unglaublich dankbar, dass ich nochmal ein Jahr mit Dir studieren, arbeiten und feiern durfte. Die intensiven (oft genug nächtlichen) Lerneinheiten mit Dir haben mein Studium geprägt.

Diese Arbeit ist nur ein Glied in einer Kette von Entwicklungen, die ich den Menschen verdanke, die meine Neugierde gefördert und mir das Selbstvertrauen geschenkt haben, dieses Studium zu meistern. Einen nicht zu unterschätzenden Beitrag dazu hat mein großartiger Physiklehrer Walter Böhm geleistet. Sein lebhafter Unterricht hat mir die nötige Inspiration für das Physikstudium geschenkt. Größter Dank geht an meine Eltern Maria und Ludwig. Ihr habt mir stets ermöglicht, meinen eigenen Weg zu gehen. Es ist fabelhaft zu wissen, dass ihr hinter mir steht. Ilona, in Deiner Schuld stehe ich besonders. Du hattest wenig von mir in letzter Zeit und es trotzdem verstanden, mir Mut, Halt und Geborgenheit zu schenken.

Appendix A.

Eccentricity of EPIC 217393088

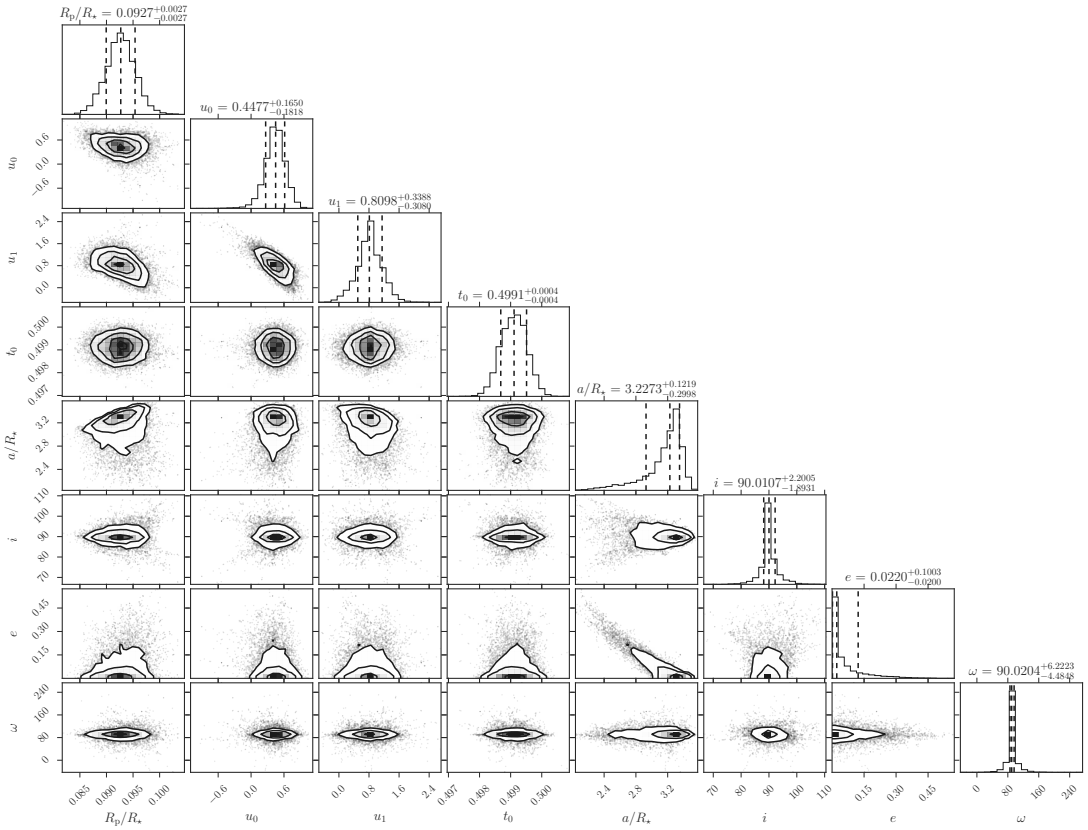

Figure A.1.: Corner plot showing posterior probability distributions (along diagonal) and covariances (off-diagonal) of all free parameters for EPIC 217393088. These posteriors were obtained from a transit fit with free e and ω. I used the beta distribution described in Section 4.3.4 as prior probability distribution.

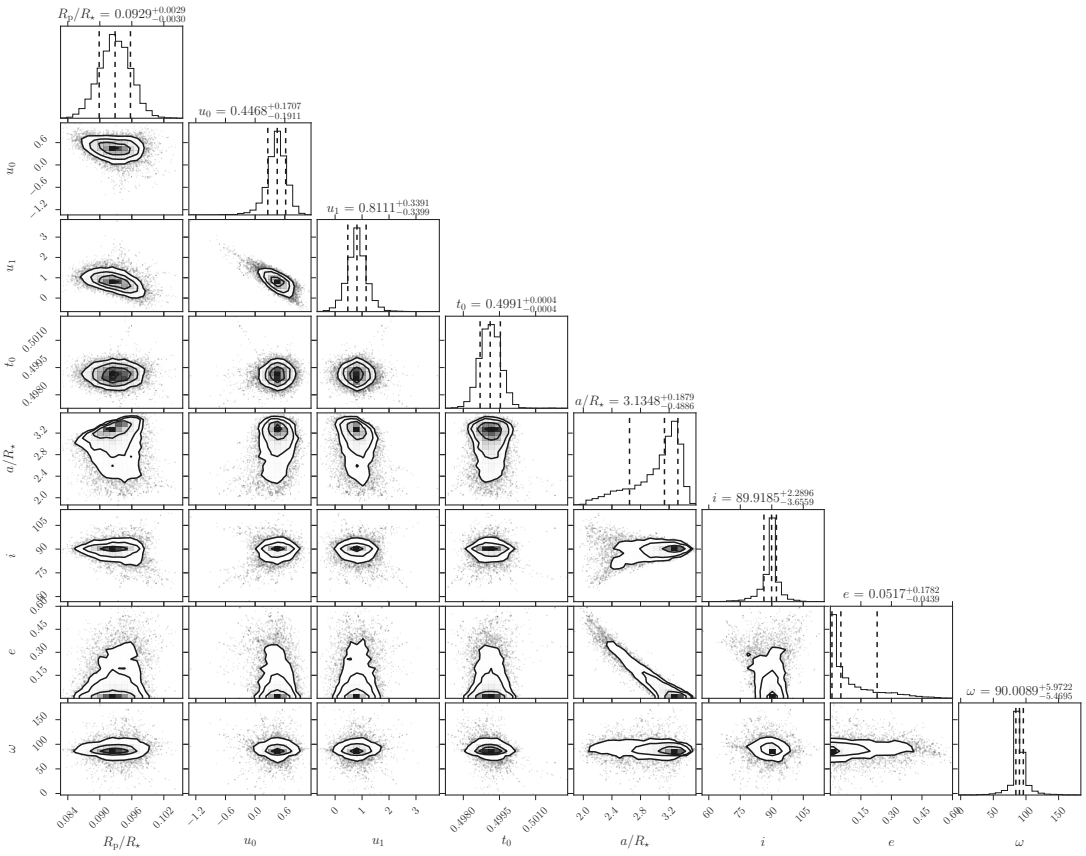

Figure A.2.: Same as Figure A.1, but using a flat prior for e.

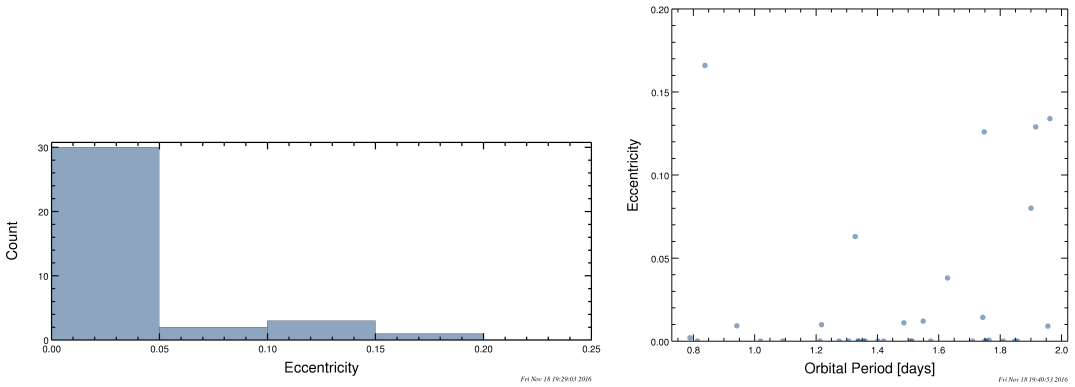

Figure A.3.: Eccentricities of confirmed short period giant planets. The sample contains only planets with $R_\mathrm{p} > 0.5 R_\mathrm{Jup}$ and $P < 2.0\,\mathrm{d}$. *Left:* Histogram of eccentricities. *Right:* Eccentricities plotted against orbital period. Planet data provided from the NASA Exoplanet Archive (Akeson et al. 2013).

Appendix B.

Contamination Check for EPIC 220262993

I checked the data of EPIC 220262993 for signs of background or foreground stars and other contaminants using the object's target pixel file (see Figure B.1) and available diagnostics of the EVEREST product (see Figure B.2).

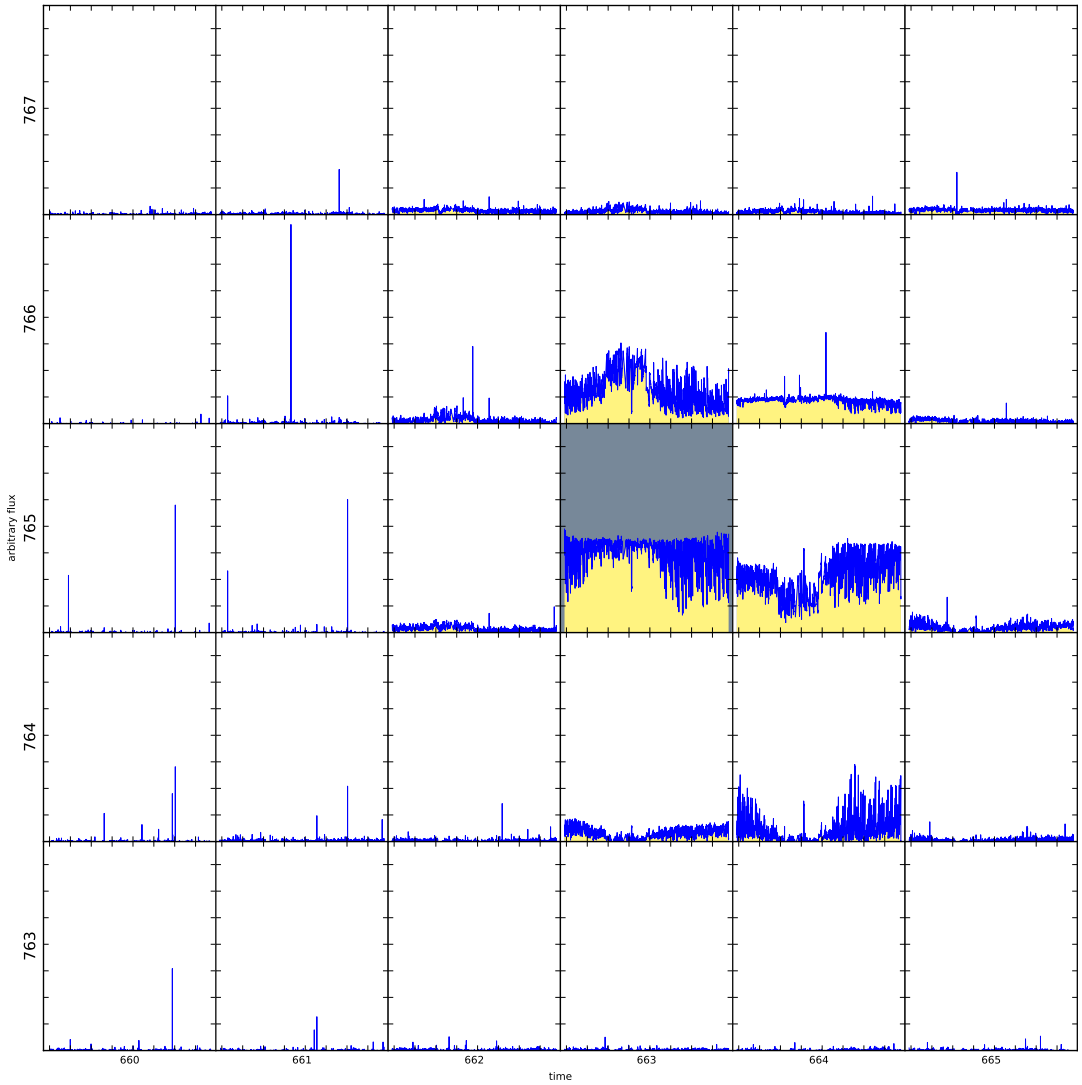

Figure B.1.: Individual pixel time series of EPIC 220262993. Blue curves show the flux time series of each individual pixel in the target mask. Only the pixel with a gray background is included in the photometric aperture used to construct the PDC light curve. There is no signature of bright companions or other contaminants visible. This plot was created from a target pixel file using the PyKE tool (Kinemuchi et al. 2012).

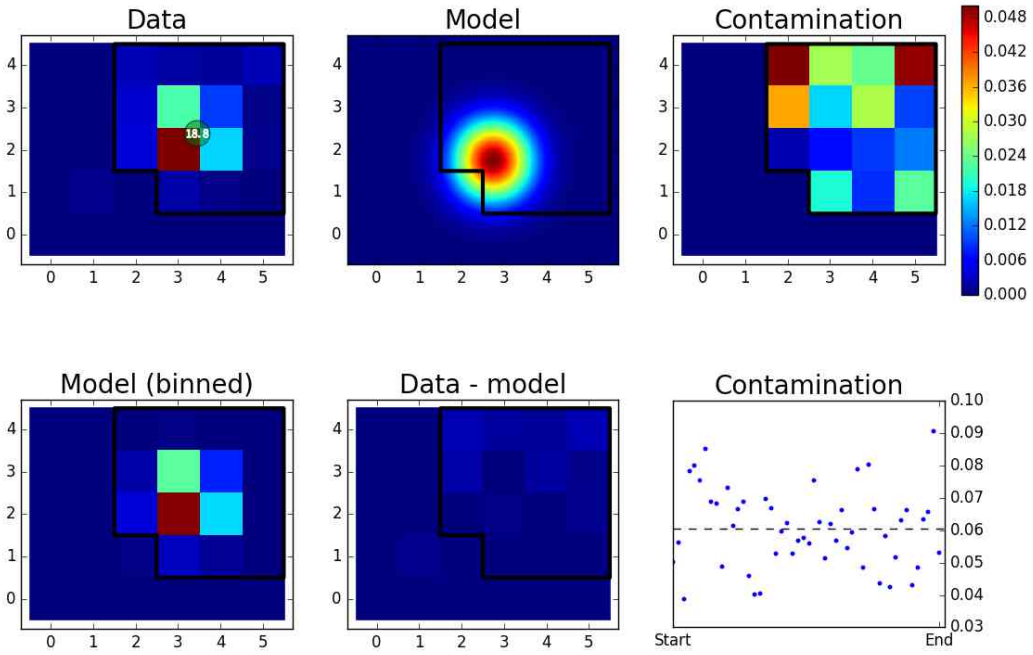

Figure B.2.: EVEREST contamination statistics for the first timestamp. The top row shows from left to right the image, an optimized PSF model, and the difference between data and model divided by the brightest pixel in the aperture. In the bottom row, a binned version of the PSF model and its difference to the data is depicted. The bottom right panel shows 50 evaluations of the contamination metric throughout Campaign 8. From these diagnostics, I did not find indications of contamination by other sources. This plot was downloaded from the MAST.